

## MASS-RADIUS RELATIONSHIPS FOR SOLID EXOPLANETS

S. SEAGER<sup>1,2</sup>, M. KUCHNER<sup>3</sup>, C. A. HIER-MAJUMDER<sup>1</sup>, B. MILITZER<sup>4</sup>  
*Draft version November 26, 2024*

### ABSTRACT

We use new interior models of cold planets to investigate the mass-radius relationships of solid exoplanets, considering planets made primarily of iron, silicates, water, and carbon compounds. We find that the mass-radius relationships for cold terrestrial-mass planets of all compositions we considered follow a generic functional form that is not a simple power law:  $\log_{10} R_s = k_1 + 1/3 \log_{10}(M_s) - k_2 M_s^{k_3}$  for up to  $M_p \approx 20M_\oplus$ , where  $M_s$  and  $R_s$  are scaled mass and radius values. This functional form arises because the common building blocks of solid planets all have equations of state that are well approximated by a modified polytrope of the form  $\rho = \rho_0 + cP^n$ .

We find that highly detailed planet interior models, including temperature structure and phase changes, are not necessary to derive solid exoplanet bulk composition from mass and radius measurements. For solid exoplanets with no substantial atmosphere we have also found that: with 5% fractional uncertainty in planet mass and radius it is possible to distinguish among planets composed predominantly of iron or silicates or water ice but not more detailed compositions; with  $\sim 5\%$  uncertainty water ice planets with  $\gtrsim 25\%$  water by mass may be identified; the minimum plausible planet size for a given mass is that of a pure iron planet; and carbon planet mass-radius relationships overlap with those of silicate and water planets due to similar zero-pressure densities and equations of state. We propose a definition of “super Earths” based on the clear distinction in radii between planets with significant gas envelopes and those without.

*Subject headings:* extrasolar planets

### 1. INTRODUCTION

The growing number and unexpected diversity of recently discovered extrasolar planets has motivated us to study the mass-radius relationship of solid exoplanets. The central question we pose is what can we determine about an exoplanet’s composition from its mass and radius? The answer to this question requires numerical models of planet interiors as well as an understanding of the current limitations and future prospects of the precision of planet mass and radius observations.

The growing number of exoplanets includes some with interesting radii. The planet HD 149026 b has such a small radius for its measured mass that the planet must have a core with a mass of 60–70  $M_\oplus$ , or 2/3 of the planet’s total mass (Sato et al. 2005). Another planet, GJ 436b, is a Neptune-mass planet (Butler et al. 2004) that was recently discovered to show transits (Gillon et al. 2007) and to have a Neptune-like radius ( $M_p = 22.6 \pm 1.9M_\oplus$  and  $R_p = 3.95 \pm 0.35R_\oplus$ ).

The unexpected diversity of exoplanets includes fourteen exoplanets with  $M_p \sin i < 21M_\oplus$  (Butler et al. 2004; McArthur et al. 2004; Santos et al. 2004; Rivera et al. 2005; Bonfils et al. 2005; Vogt et al. 2005; Lovis et al. 2006; Udry et al. 2006; Bonfils et al. 2007; Melo et al. 2007), including one with  $M_p = 7.5M_\oplus$  (Rivera et al. 2005) and another with  $M_p = 5M_\oplus$  orbiting at the in-

ner edge of its host star’s habitable zone (Udry et al. 2007). Microlensing surveys have discovered two low-mass planets,  $\sim 5.5M_\oplus$  (Beaulieu et al. 2006) and  $\sim 13M_\oplus$  (Gould et al. 2006) at  $\sim 2.5$  AU from their parent stars, suggesting that Neptune-mass planets are common. In one planetary system, the Neptune-mass planet is the most massive planet in the system (Gould et al. 2006).

Space-based missions provide us with further motivation for our study. COROT<sup>5</sup> (CNES; launched 27 December 2006) and Kepler<sup>6</sup> (NASA; launch date 2008) will search for low-mass exoplanets that transit their host star. GAIA<sup>7</sup> (ESA; launch date 2011) will measure stellar distances (and hence their radii) precisely, removing a limiting factor in deriving a precise planetary radius. Ground-based radial velocity techniques are pushing to higher precision, and will enable mass measurements of many of the COROT and Kepler planets.

To examine what can we determine about an exoplanet’s composition from measurements of its mass and radius, we derive theoretical mass-radius relationships for a wide range of exoplanet masses. To explore a wide range of masses and compositions, we make a major simplification: we make the approximation that the planet is at a uniform low temperature. This approximation of uniform low temperature serves as a practical simplification because the equations of state (EOSs) are relatively well described at

<sup>1</sup> Department of Terrestrial Magnetism, Carnegie Institution of Washington, 5241 Broad Branch Rd. NW, Washington, DC 20015

<sup>2</sup> Department of Earth, Atmospheric, and Planetary Sciences, Department of Physics, Massachusetts Institute of Technology, 54-1626, 77 Massachusetts Ave., Cambridge, MA, 01742

<sup>3</sup> Exoplanets and Stellar Astrophysics Laboratory, Code 667, NASA/Goddard Space Flight Center, Greenbelt, MD 20771

<sup>4</sup> Geophysical Laboratory, Carnegie Institution of Washington, 5251 Broad Branch Rd. NW, Washington, DC 20015

<sup>5</sup> <http://smsc.cnes.fr/COROT/>

<sup>6</sup> <http://kepler.nasa.gov/>

<sup>7</sup> <http://sci.esa.int/science-e/www/area/index.cfm?fareaid=26>

zero-temperature or at 300 K for a wide variety of materials below 200 GPa. The full temperature-dependent EOSs for the materials of interest are either unknown or highly uncertain at the temperatures massive solid planets can reach in their interiors and in the pressure range beyond the reach of static compression experiments ( $\lesssim 200$  GPa) and the analytical high pressure laws of plasma physics ( $\gtrsim 10^4$  GPa).

We adopt our approach from the foundational work of Zapolsky & Salpeter (1969) who computed mass-radius relationships for homogeneous zero-temperature spheres of single elements. We improve upon Zapolsky & Salpeter (1969) by using a more accurate EOS at pressures  $P \lesssim 1000$  GPa. We further expand upon Zapolsky & Salpeter (1969) by: considering more realistic planetary materials; considering differentiated planets; by exploring the effects of temperature on the planet mass and radius; and by investigating potential observational uncertainties on planet mass and radius.

This work complements the highly focused physical models of low-mass exoplanets offered by other authors. A detailed study by Léger et al. (2004) focused on water planets, and provided a detailed model of the interior and atmosphere of a  $6 M_{\oplus}$  planet with an interior composition of:  $3 M_{\oplus}$  of water,  $2 M_{\oplus}$  of a silicate mantle and  $1 M_{\oplus}$  iron and nickel core (see also Kuchner (2003) for a description of a water planet.) Valencia et al. (2006) calculated the mass-radius relationship for “super Earths” and “super Mercuries” (defined in their paper to be  $1\text{--}10 M_{\oplus}$  and similar composition to Earth and  $1\text{--}10$  Mercury masses and similar composition to Mercury, respectively). Valencia et al. (2006) explore different mineral compositions of the mantle and core, and investigate whether the planets have solid or liquid cores and apply their model to Gl 876d in Valencia et al. (2007b) and to degeneracies of planet interior composition in Valencia et al. (2007a). Ehrenreich et al. (2006) model small cold exoplanets to study the microlensing planet OGLE 2005-BLG-390Lb (Beaulieu et al. 2006). In the past Stevenson (1982) and more recently Fortney et al. (2007) and Sotin et al. (2007) have also investigated mass-radius relationships of rocky and icy exoplanets.

We take a broader view than these previous studies using more approximate models in order to investigate planets of a wide range of compositions and masses. We describe our model in §2 and the equations of state (EOS) in §3. In §4 we present mass-radius relationships for homogeneous and differentiated planets, and discuss the effects of phase changes and temperature. In §5 we describe a generic mass-radius relationship shared by all solid exoplanets under our approximation. We discuss the broad consequences of our study in §6 followed by a summary and conclusion in §7.

## 2. MODEL

We solve for  $m(r)$ , the mass contained within radius,  $r$ ,  $P(r)$ , the pressure, and  $\rho(r)$ , the density of a spherical planet from three equations: the mass of a spherical shell

$$\frac{dm(r)}{dr} = 4\pi r^2 \rho(r); \quad (1)$$

the equation of hydrostatic equilibrium

$$\frac{dP(r)}{dr} = \frac{-Gm(r)\rho(r)}{r^2}; \quad (2)$$

and the equation of state (EOS)

$$P(r) = f(\rho(r), T(r)), \quad (3)$$

where  $f$  is a unique function for a given material. Different approximations to the EOS have been derived and we describe our choice in detail in §3. For the majority of the calculations for solid materials presented here, we neglect the temperature dependence of the EOS and use experimental data obtained at room temperature. The importance of thermal contributions to the pressure are discussed in §4.2.2.

We numerically integrate equations (1) and (2) starting at the planet’s center ( $r = 0$ ) using the inner boundary condition  $M(0) = 0$  and  $P(0) = P_{\text{central}}$ , where  $P_{\text{central}}$  is a chosen central pressure. For the outer boundary condition we use  $P(R_p) = 0$ . The choice of  $P_{\text{central}}$  at the inner boundary and the outer boundary condition  $P(R_p) = 0$  defines the planetary radius  $R_p$  and total mass  $M_p = m(R_p)$ . Integrating equations (1) and (2) over and over for a range of  $P_{\text{central}}$  provides the mass-radius relationship for a given EOS.

For differentiated planets containing more than one kind of material, we specify the desired fractional mass of the core and of each shell. We then integrate equations (1) and (2) as specified above, given a  $P_{\text{central}}$  and outer boundary condition. We switch from one material to the next where the desired fractional mass is reached, using a guess of the total planet mass. Since we do not know the total mass that a given integration will yield ahead of time, we generally need to iterate a few times in order to produce a model with the desired distribution of material.

We tested our code by trying to duplicate the mass-radius curves in Zapolsky & Salpeter (1969), using their EOS (Salpeter & Zapolsky 1967). Our mass-radius curves agreed with those in Zapolsky & Salpeter (1969) to within a few percent.

## 3. EQUATIONS OF STATE

An equation of state (EOS) describes the relationship between density, pressure, and temperature for a given material in thermodynamic equilibrium. Because we compute models without temperature dependence, we choose a form of EOS that assumes uniform or zero temperature. For  $P \lesssim 200$  GPa we use fits to experimental data, either the Vinet EOS or the Birch-Murnaghan EOS (BME). For  $P \gtrsim 10^4$  GPa, where electron degeneracy pressure becomes increasingly important we use the Thomas-Fermi-Dirac theoretical EOS. In between these pressures the EOSs are not well known and we treat the EOS as described in §3.3.

### 3.1. Low-Pressure EOSs: Vinet and Birch-Murnaghan

For pressures below approximately 200 GPa we rely on experimental data which have been fit to the common EOS formulae of either Vinet (Vinet et al. 1987, 1989) or BME (Birch 1947; Poirier 2000). For a derivation of these EOSs see Poirier (2000). The Vinet EOS is

$$P = 3K_0\eta^{2/3} \left[ 1 - \eta^{-\frac{1}{3}} \right] \exp \left( \frac{3}{2}(K'_0 - 1) \left[ 1 - \eta^{-\frac{1}{3}} \right] \right), \quad (4)$$

and the third order finite strain BME is

$$P = \frac{3}{2}K_0 \left[ \eta^{\frac{7}{3}} - \eta^{\frac{5}{3}} \right] \left\{ 1 + \frac{3}{4}(K'_0 - 4) \left[ \eta^{\frac{2}{3}} - 1 \right] \right\}. \quad (5)$$

For the 4th order finite strain BME, the term

$$+ \frac{3}{2} K_0 \left[ \eta^{\frac{7}{3}} - \eta^{\frac{5}{3}} \right] \frac{3}{8} K_0 \left( \eta^{2/3} - 1 \right)^2 \quad (6)$$

$$\times \left[ K_0 K_0'' + K_0' (K_0' - 7) + \frac{143}{9} \right]$$

is added to equation (5). Here  $\eta = \rho/\rho_0$  is the compression ratio with respect to the ambient density,  $\rho_0$ .  $K_0 = -V \left( \frac{\partial P}{\partial V} \right)_T$  is the bulk modulus of the material,  $K_0'$  is the pressure derivative, and  $K_0''$  is the second pressure derivative. The majority of experiments (from which  $K_0$  and  $K_0'$  are derived) are typically limited to pressures less than 150 GPa and temperatures less than 2000 K.

Both the BME and the Vinet EOSs are empirical fits to experimental data. The Vinet EOS is considered to be more suitable than the BME EOS for extrapolation to high pressures, because the BME is derived from an expansion of the elastic potential energy as a function of pressure truncated to low orders (Poirier 2000). Where possible we choose the Vinet or BME fit provided for experimental data according to which fit best matches up with the TFD EOS at high pressures. In one case we used a fourth order BME where the term  $K_0''$  is determined theoretically (see §3.3). Table 1 lists the  $K_0$ ,  $K_0'$ , and the type of EOS fit we used for each material.

### 3.2. High-Pressure EOS: Thomas-Fermi-Dirac

The Thomas-Fermi-Dirac (TFD) theory was derived in the late 1920s as an approximate way to characterize the interactions of electrons and nuclei. The electrons are treated as a gas of noninteracting particles that obey the Pauli exclusion principle and move in the Coulomb field of the nuclei. Under the assumption that the potential is slowly varying, a self-consistent solution is derived so that Pauli exclusion pressure balances out the Coulomb forces (Eliezer et al. 2002).

These approximations lead to a comparatively simple description that works for any material and becomes increasingly accurate at high pressure. For each material, however, there is a pressure limit below which the TFD model is no longer valid, where the assumption of a noninteracting electron gas in a slowly varying potential breaks down. In real materials, the electrons occupy well-defined orbitals, which leads to chemical bonds and determines the crystal structure as a function of pressure and temperature. The TFD theory cannot describe chemical bonds and is insensitive to the arrangements of atoms in a particular structure. At very high pressure, however, where the kinetic energy dominates over the Coulomb energy, all these effects become less important and TFD theory yields an increasingly accurate EOS.

In this paper, we use a modified TFD theory developed by Salpeter & Zapolsky (1967). The authors extended the original TFD theory by adding a density dependent correlation energy term that captures some of the interaction effects of the electrons. In all of the following TFD calculations, we included the correlation energy correction calculated with fit formulae provided in Salpeter & Zapolsky (1967)<sup>8</sup>. We also follow this paper for the description of mixtures of different types of atoms.

Since the TFD theory does not describe chemical bonds it does not reproduce the correct zero-pressure density, and can even be in error by up to a factor of two or more (Zapolsky & Salpeter (1969); see Figure 1). Instead we rely on experimental data for lower pressure, which are available for almost all materials we consider.

### 3.3. Intermediate-Pressure EOS and Details for Specific Materials Used

The pressure range from approximately 200 to 10<sup>4</sup> GPa is not easily accessible to experiment nor is it well described by the TFD EOS. Although shock experiments can reach pressures over 1000 GPa, a substantial contribution to the pressure comes from the thermal pressure (see §4.2.2) because the material is also heated under shock compression. When a shock wave passes through a solid material, its density is only increased by up to a factor of 4. It is this limited compression ratio, which makes it very difficult to obtain low temperature EOS data beyond 200 GPa, the range needed to model planetary interiors. For all materials but H<sub>2</sub>O in this pressure regime we simply use the Vinet/BME EOS up until the point where it intersects the TFD EOS curve, and the TFD EOS at higher pressures (see Figure 1). A more accurate EOS in the intermediate pressure range 200 to 10<sup>4</sup> GPa range demands new theoretical calculations. Such EOSs are not readily available since there are almost no applications that require EOSs in this pressure range.

**Water Ice:** As an example of how to fill this gap we used density functional theory to calculate the EOS of water ice in the phases VIII and X in the pressure range 2 to 7700 GPa (Figure 3 and Table 2). The theoretical EOS data presented here are in agreement with water ice VII experimental data (Hemley et al. 1987) in the range 6 to 127 GPa to within 3.5% in density for a given pressure. Our Vinet fit to the combined theoretical data for water ices VIII and X has parameters  $\rho_0 = 1460 \text{ kg/m}^3$ ,  $K_0 = 14.3771 \text{ GPa}$ , and  $K_0' = 6.57972$ . This fit deviates from the tabular data in Table 2 by less than 2.5% in density for a given pressure.

At  $P > 3$  to 20 GPa water ice is in either phase VII or VIII, depending on temperature (see the water phase diagram in, e.g., Petrenko & Whitworth (1999)). The structure of water ice phases VII and VIII are extremely similar, differing only by the ordering of the hydrogen atom. This different structure causes a negligible difference in the EOS, making the experimental water ice VII and the theoretical VIII EOS comparable. At  $P = 60 \text{ GPa}$  water ice VII/VIII undergoes a phase change to water ice X. In this structure, the distinction between covalent bonds and hydrogen bonds goes away. Instead the hydrogen atom shifts to the mid-point between two oxygen atoms, while the hydrogen atoms occupy off-center sites in all ice structures at lower pressures. More details on our choices of EOSs follow.

For this work we adopt the following for our water EOS. We use the BME fit from the Hemley et al. (1987) water ice VII data up to  $P = 44.3 \text{ GPa}$ . At this pressure the theoretical data and the experimental data agree precisely.

<sup>8</sup> Note that the denominator in the second term of  $\phi$  as defined in Salpeter & Zapolsky (1967) is listed as  $4.3^{1/3}$ ; the factor  $4 \times 3^{1/3}$  actually reproduces the EOSs in their paper. This definition of  $\phi$  differs from the one in Zapolsky & Salpeter (1969), which appears to be missing a factor of  $1/3^{1/3}$ .

Starting at  $P = 44.3$  GPa we use the theoretical data derived from density functional theory, which represent state-of-the-art first-principles calculations. These calculations were performed with the Vienna *ab initio* simulation package using the projector augmented-wave method (Kresse & Furthmüller 1996). The calculations predict a gradual transformation from ice VIII to X. The resulting EOS is given in Table 2. At a pressure of 7686 GPa, our density functional theory calculation agrees with the TFD model and we use this pressure to switch to TFD for all higher pressures. In principle, density functional theory calculations can be performed for any material with a known crystal structure—this provides a way to bridge the gap in pressure between the experimental data and the TFD limit.

For the liquid water EOS for  $P \leq 10$  GPa, we use the logarithmic EOS (see, e.g., Poirier 2000). We use  $K_0 = 2.28$  GPa for seawater at  $12^\circ$  K from Halliday et al. (2003).

**Iron:** For an Fe EOS we use the  $\epsilon$  phase of Fe with a Vinet fit up to  $P = 2.09 \times 10^4$  GPa. Note that the Vinet fit parameters are from experimental data with  $P \leq 330$  GPa Anderson et al. (2001). At this pressure the Vinet curve smoothly approaches the TFD EOS, and we switch to the TFD EOS.

**Silicate:** For a silicate EOS we use the perovskite phase of  $\text{MgSiO}_3$ . We use a fourth order BME fit up to  $P = 1.35 \times 10^4$  GPa. At this pressure we switch to the TFD EOS. The fourth order BME fit is from a density functional calculation up to  $P = 150$  GPa by Karki et al. (2000). Karki et al. (2000) note that their  $K'_0$  agrees with fits to experimental data from several sources and  $K_0$  is within the range of experimental data (247 GPa compared to 246–272 GPa). The advantage of the Karki et al. (2000) fit parameters is that the fourth order BME is the only fit we found that smoothly matches the TFD EOS at high pressures.

**Other materials:** Other materials used in this work include MgO (Duffy et al. 1995),  $(\text{Mg,Fe})\text{SiO}_3$  (Knittle & Jeanloz 1987), and SiC (Alexsandrov et al. 1989). For these species we use the BME fit up to the pressure where they intersect the TFD curve.

Carbon was the only material we used whose Vinet EOS and TFD EOS did not intersect; this was likely because we only considered the graphite phase at pressures below the TFD EOS. For graphite we interpolated between the Vinet and TFD EOS. For H, He and the carbon monoxide EOS, we used the TFD EOS at all pressures, for simplicity. We set the density to a constant at the low pressures ( $P < 10^8$  Pa) where the TFD EOS is poorly behaved. We note that a CO EOS from shock experiments exists (Nellis et al. 1981) in the pressure range 5 to 60 GPa, and it has a density to within eight to sixteen percent of our TFD density. Our CO EOS and mass-radius relationship is therefore approximate.

#### 4. NUMERICAL RESULTS

We now describe our numerical solutions to equations (1) through (3) using our assembled collection of EOSs. We used our model to investigate the mass-radius relationships for planets from  $0.01$ – $1000 M_\oplus$ . The lower mass limit encompasses planets as small as Mercury and small

bodies like the icy moons of Jupiter and Saturn. The upper-mass limit encompasses the 13 Jupiter-mass planet limit. Above this mass, self-gravitating H-He spheres undergo deuterium or sustained hydrogen fusion (depending on how massive the body is) and are not considered planets.

#### 4.1. Mass-Radius Relationships

##### 4.1.1. Homogeneous Planets

Building upon Zapolsky & Salpeter (1969), we first consider planets of uniform composition. This artificial scenario helps us understand the fundamental properties of the planet mass-radius relationships. Figure 4 shows the mass-radius relationship for homogeneous planets of H, H/He (25% He by mass),  $\text{H}_2\text{O}$  (ice),  $\text{MgSiO}_3$  (perovskite), and Fe.

Homogeneous planets all show the same general trend in radius as a function of mass. For  $M_p \lesssim 500 M_\oplus$  the planets' radii increase with increasing mass. In this regime, Coulomb forces balance gravity in hydrostatic equilibrium. For large masses,  $M_p \gg 500 M_\oplus$ , the compression in the interior is high enough to pressure ionize the atoms. At these large masses degeneracy pressure of free electrons balances gravity in hydrostatic equilibrium, and as more mass is added to the planet, the planet shrinks (Hubbard 1984). Although planets are not fully degenerate (the term is reserved for stellar mass white dwarfs (Chandrasekhar 1939)), electron degeneracy pressure does have a significant effect on the mass-radius relationship for high planetary masses over  $500 M_\oplus$ . In particular, planets of all compositions are approximately the same size for a decade of mass where the competing effects of Coulomb forces (which cause  $R_p \sim M_p^{1/3}$ ) and electron degeneracy pressure ( $R_p \sim M_p^{-1/3}$ ) roughly cancel each other out. See Zapolsky & Salpeter (1969) for a detailed discussion of the maximum radius for a given planet of homogeneous composition.

If we assume that our selection of materials spans all plausible major planet materials, then we can make some inferences from Figure 4 about the range of planet sizes. First, the Fe-planet mass-radius relationship shows the minimum radius a planet of a given mass can possess. Second, since water is the least dense of all the materials we studied (apart from H and He), the water planet curve in Figure 4 may serve to show the maximum radius for a planet with no substantial atmosphere.

The mass-radius relationships for planets of homogeneous compositions (Figure 4) can be used to infer the bulk composition of planets. Using the solar system as an example, and from Figures 4 and 5, we could infer that Earth and Venus are composed primarily of a mixture of silicates and iron, while Mercury is composed predominantly of iron. We could also infer that Uranus and Neptune are not giant H/He planets and nor are they “rock giants”; they are predominantly rocky or icy and must have small but significant gas envelopes. Jupiter and Saturn are grossly fit by the H/He curve, but the H/He interiors of hot Jupiters are dominated by thermal effects and are thus not fit well by cold homogeneous planets; indeed we are not aiming to model gas giant planets in this paper.

Turning to exoplanets, Figure 4 shows that the transit-

ing Saturn-mass<sup>9</sup> exoplanet HD 149026b must contain a substantial fraction of elements heavier than H and He. More detailed evolutionary and interior models find that HD 149026b has  $70 M_{\oplus}$  of rocky material, almost 2/3 of its total mass (Sato et al. 2005). At  $22.6 M_{\oplus}$  and  $3.95 R_{\oplus}$ , GJ 436b must have a significant H/He envelope because its radius is clearly larger than a pure water ice planet. The  $7.5 M_{\oplus}$  planet Gliese 876d (Rivera et al. 2005) does not have a measured radius, but a radius measurement with a fractional radius uncertainty of 5% would distinguish among a predominantly rocky planet, a predominantly icy planet and a planet with a substantial gas envelope.

We have modeled massive solid exoplanets up to  $4000 M_{\oplus}$  (up to 13 Jupiter masses). These planets would be Jupiter-mass planets composed of solid material. Such massive exoplanets are not yet known to exist. In the standard planet formation theory massive planets are primarily composed of H/He and are limited to have rocky/icy cores of up to about  $10M_{\oplus}$ . HD 149026b with a  $70 M_{\oplus}$  core shows that a wider range of planets exist. Massive solid exoplanets of hundreds to thousands of Earth masses may be able to form around massive stars (B and O stars;  $5\text{--}120 M_{\odot}$ ) where the protoplanetary disk would contain enough heavy elements. Additionally these stars have high UV radiation and winds which could photoevaporate the nascent protoplanetary gas disk, allowing massive planets to form out of the remaining solid material.

#### 4.1.2. Differentiated Planets

All solar-system planets have multiple layers of different compositions. These planets are differentiated, meaning the denser material lies beneath shells of progressively less dense material. We now consider differentiated planets of various compositions. We focus on materials that comprise the solar system planets and moons: iron, silicates,  $\text{H}_2\text{O}$  (ice), and H/He gas envelopes. We ignore elements that have abundances too low to affect our model for the planet radius.

We explore two types of differentiated gas-free planets, iron/silicate planets and water planets. These planets lack gas envelopes, although they may have atmospheres too small to affect the measured planet radius. Figure 4 shows the mass-radius relationship for differentiated planets without gas envelopes. Figure 5 shows the same mass-radius relationships in more detail. The calculations assume a constant fractional mass in each layer. In general, the radii of differentiated planets (where the more dense components are interior to the less dense components) lie in between the radii of homogeneous spheres composed of the planet’s most and least dense components.

We investigate iron/silicate planets with iron cores and  $\text{MgSiO}_3$  mantles. We consider Fe core mass fractions of 32.5% (“super Earths”) and 70% (“super Mercuries”). It is remarkable how well Mercury, Venus, and Earth’s masses and radii are fit by these cold iron/silicate planets, as seen in Figure 5. We show the density as a function of radius for the silicate planets in Figure 6a and b. As expected, the more massive planets have higher densities in their cores.

<sup>9</sup> Saturn is  $95 M_{\oplus}$  and Jupiter is  $318 M_{\oplus}$ .

<sup>10</sup> Under a water planet definition that includes H/He envelopes, Uranus and Neptune would also be water planets, because they are believed to have  $> 25\%$  water by mass.

We define water planets to be solid planets with  $> 25\%$   $\text{H}_2\text{O}$  by mass. Jupiter’s moons Ganymede and Callisto would be water planets by this definition<sup>10</sup>. We investigate water planets with iron cores and silicate mantles. We consider planets with fixed mass fractions: 45% water, 48.5% silicates and 6.5% Fe (similar to Jupiter’s icy moon Ganymede (Schubert et al. 2004)); 75% water and 22% silicates and 3% iron (the core and silicate shell mass ratio as Ganymede); and 25% water with a 58% silicate shell and a 17% iron core. Figure 6c shows the density profiles as a function of planet radius for the 45% water planets.

We compared our fiducial super-Earth model with a 32.5% Fe core and 67.5% silicate mantle to a model that more closely represents Earth: a model with a 32.5% by mass core of FeS (where FeS includes 10% S by mass) and a mantle that includes 90%  $(\text{Mg,Fe})\text{SiO}_3$  and 10% MgO (Poirier 2000). The results from this Earth model are shown by the squares in Figure 7 and agree closely with our fiducial super-Earth-like planet. It is remarkable how our simple fiducial model matches the Earth’s radius to within three percent for a  $1M_{\oplus}$  planet.

There are further degeneracies among the mass-radius relationships for planets of different compositions. For example, planets with 10% water by mass (with 27% iron cores and 63% silicate mantles) have mass-radius curves that overlap with our silicate planet mass-radius curves. As a second example, if we adopt a  $6 M_{\oplus}$  water planet similar to the Léger et al. (2004) water planet composed of  $1 M_{\oplus}$  Fe,  $2 M_{\oplus}$  silicates, and  $3 M_{\oplus}$   $\text{H}_2\text{O}$ , we find the total planet radius differs by less than 0.5% from that of our model with 45% water, 48.5% silicates, and 6.5% Fe. While the total planet mass and radius are the same, the interior structure of the models are quite different, as shown in Figure 7d (but note that the interior structure of our Leger-type planet is different than the one in (Léger et al. 2004)). For the same mass, the radius of the Leger-type planet will be slightly lower, but both types of planets fall along the same mass-radius curve. See Valencia et al. (2007a) and Li et al. (in prep) for detailed discussions on degeneracies in planets composed of iron cores, silicate mantles, and water outer layers.

#### 4.1.3. Planets with H/He Gas Envelopes

We now turn to a discussion of differentiated planets with significant H/He envelopes. For simplicity and consistency, we use a zero-temperature EOS for H and He (Salpeter & Zapolsky 1967). A zero-temperature EOS for a H/He mixture may represent real planets only poorly, but since a zero temperature EOS underestimates a gas’s volume, using such an EOS allows us to one important point: adding a H/He shell can easily boost a planet’s radius dramatically. For example, adding 20% H/He by mass can double a planet’s radius.

Figure 8 shows mass-radius relationships for planets with gas envelopes and fixed core masses. The cores contain 70%  $\text{MgSiO}_3$  and 30% Fe. Five cases are shown: planets with fixed core masses of 5, 10, 20, 50, and  $100 M_{\oplus}$ . The values in Figure 8 are lower limits because thermal

effects will move the gas curves up and left, i.e. to larger radii. For a detailed discussion of mass-radius curves for planets with significant gas envelopes see Fortney et al. (2007) and Adams et al. in preparation. In Figure 8 we also show the radius of the core of the H/He planets as a function of the total mass of the fixed-mass core and overlying H/He envelope.

All planets with a significant amount of H/He will have a larger radius than the homogeneous water ice planets. Planets with even a relatively small fractional mass of H/He can therefore be distinguished from planets with an insignificant gas envelope (Figure 8). Uranus and Neptune, for example, are believed to have about 10% of their mass in H/He material. Yet, Uranus and Neptune are up to two times larger than a planet of similar mass and core composition but without the H/He envelope. We propose to call planets without a significant gas envelope — i.e. planets that lie below the pure water ice line—super Earths.

#### 4.1.4. *Non-Standard Planets: Carbon and Helium Planets*

We now consider planets with compositions very different from solar system planets, beginning with carbon planets. We have previously presented the idea of carbon planets, planets composed of  $> 50\%$  carbon compounds by mass (Kuchner & Seager (2006); See also Cameron et al. (1988) and Gaidos (2000)). Carbon planets should form in environments where the carbon-to-oxygen ratio  $C/O \gtrsim 1$ , in contrast to the solar abundance ratio ( $C/O = 0.5$ ). When  $C/O \gtrsim 1$ , the high-temperature condensates available in chemical equilibrium are very different from the environment with  $C/O < 1$  (Lewis 1974; Wood & Hashimoto 1993; Lodders & Fegley 1997). For example, SiC is the dominant form of Si instead of silicates (i.e., Si-O compounds). Such carbon-rich environments may occur in a local area enriched in C or depleted in  $H_2O$  in an otherwise solar-abundance protoplanetary disk. Carbon-rich environments would also occur in a protoplanetary disk with a global  $C/O > 1$  like the disk that formed the planets around pulsar PSR 1257+12 (Wolszczan & Frail 1992), and do occur in the well-known Beta Pictoris debris disk (Roberge et al. 2006).

The dominant composition of carbon planets is unknown. The details would depend on protoplanetary disk temperature, composition, relative abundance and departures from chemical equilibrium. SiC and graphite are both plausible compositions (based on observations and calculations of carbon star atmospheres; Lodders & Fegley (1997)). We compute the mass-radius relationship for three different kinds of carbon planets. The first carbon planet is a planet with an Fe core and an SiC mantle. The second is a carbon planet with an Fe core and a graphite mantle. The third type of carbon planet is a pure CO (carbon monoxide) planet. A carbon monoxide planet could form in a stellar disk composed from a CO white dwarf that has been shredded by its more massive stellar binary companion (Livio et al. 1992).

The main result from our carbon planet computations (Figure 9) is that the carbon planet mass-radius relationships overlap those of the silicate and water planets. This is because the zero-pressure density of SiC ( $3.22 \text{ g/cm}^3$ ) is

similar to that of  $MgSiO_3$  ( $4.10 \text{ g/cm}^3$ ). While the zero-pressure density of graphite ( $2.25 \text{ g/cm}^3$ ) is almost twice that of water ice VII ( $1.46 \text{ g/cm}^3$ ), a graphite planet with an Fe core has a similar average density to a water planet with an iron core and silicate mantle. CO planets' mass-radius curves also overlap the mass-radius curves of water planets that contain iron and silicate because of a similar zero-pressure density. Our CO planets are similar in average density to water ice planets, again because the zero pressure densities are similar. The precise mass-radius relationship of CO planets should involve temperature, and a more accurate EOS than our adopted one.

We also compute the mass-radius relationship for a pure He planet. We again use the zero-temperature He EOS (Salpeter & Zapolsky 1967) to avoid introducing a free parameter based on the planet's unknown entropy. The helium mass-radius relationship is therefore approximate.

A predominantly He planet may potentially form from a low-mass white dwarf. For example, a He planet can conceivably form in one type of symbiotic binary star called an AM CVn (AM Canes Venatici), composed of two very H-poor white dwarfs (i.e., He core white dwarfs) surrounded by a circumbinary helium accretion disk formed during mass transfer from the less massive to the more massive white dwarf (see, e.g., Podsiadlowski et al. (2003), and references therein). After it loses most of its mass, the less-massive WD may approach planetary mass.

#### 4.2. *Phase Changes and Thermal Effects*

Real planets have phase changes and temperatures above 300 K in their interiors. Here we investigate the effect of phase changes and temperatures on the planet mass and radius. While models that include temperature and phase changes can be more realistic than our simple models, they complicate the interior boundary conditions and necessarily involve regimes where the EOSs are highly uncertain. See Léger et al. (2004); Valencia et al. (2006); Selsis et al. (2007); Sotin et al. (2007); Valencia et al. (2007b) for low-mass planet interior models that do include phase and temperature changes for specific types of planets.

##### 4.2.1. *Phase Changes*

In this section we show that the low-pressure phase changes have little effect on the planet mass-radius curves. This lack of effect is because the low-pressure phase changes occur at pressures  $< 10 \text{ GPa}$ . Figure 11 shows the pressure at  $m(r) = 0.97M_p$  for homogeneous planets. Figure 11 shows that for planets  $\gtrsim 3M_\oplus$ , most of the planet's mass is at pressures higher than 3 GPa (with the exception of pure water planets). Here we discuss the phase changes in some of the key planetary materials individually.

**Water:** We begin by investigating the liquid water to water ice phase change. The room-temperature bulk modulus  $K_0$  for liquid water is an order of magnitude smaller than  $K_0$  for water ice VII. Furthermore, the densities of liquid water and water ice VII are different by 50% (see Table 1). Despite these large differences in physical properties, it is important to remember that liquids are still not highly compressible materials and we expect them to behave more similarly to solids than to gases under high pressure. In order to investigate the effect of a liquid water phase for a water planet, we consider liquid water to

be present at  $P < 10$  GPa. The temperature would be  $\sim 650$  K for water to remain a liquid at this high pressure. We consider the differences between a pure water ice planet with and without the liquid ocean. We find less than three percent difference in the radius for water ice planets without and with a liquid water ocean for planets in the mass range 1 to  $4 M_{\oplus}$ . We find  $< 1\%$  difference in the radii of the two types of planets for  $M_p$  above  $5 M_{\oplus}$  (see Figure 7).

**Silicates:** We now turn to phase changes in our  $\text{MgSiO}_3$  perovskite planets by considering the low-pressure phase of  $\text{MgSiO}_3$  called enstatite. We adopt the low-pressure enstatite phase at pressures less than 10 GPa. The difference in  $K_0$  and  $\rho_0$  between the high-pressure perovskite phase and the low-pressure enstatite phase are much less than the differences between liquid water and water ice (see Table 1). Hence, just as in the water planet case, we see a relatively small difference ( $< 1\%$ ) in radius between silicate perovskite planets with and without a layer of enstatite at  $P \leq 10$  GPa (see Figure 7).

**Iron:** We now turn to phase changes in Fe. The low-pressure phase of Fe is  $\text{Fe}(\alpha)$ .  $\text{Fe}(\varepsilon)$  and  $\text{Fe}(\alpha)$  have the same  $K_0$  and  $K'_0$  to within the experimental error bars, and only slightly different zero-pressure densities (see Table 1). Additionally,  $\text{Fe}(\alpha)$  only exists at  $< 10$  GPa; whereas in a differentiated planet Fe is expected to exist at pressures higher than 10 GPa and in a homogeneous Fe planet most of the planet's mass is above 10 GPa (Figures 10 and 11). For these reasons the phase change of  $\text{Fe}(\alpha)$  to  $\text{Fe}(\varepsilon)$  has little to no effect on the mass-radius relationship of Fe planets.

**High pressure phase changes:** Even if there is a phase change at high pressures (not considered here), we expect the associated correction to the EOS to be small, and hence the derived planet radii to be reasonably accurate. Phase changes arise from a rearrangement of atoms in the crystal structure and the associated modifications in chemical bonds. With increasing pressure, the atoms become packed more and more efficiently and the importance of chemical bonding patterns drops significantly. For example, above 100 GPa, the postperovskite phase (Murakami et al. 2004) and perovskite phase of silicate have very similar zero pressure volumes and bulk moduli, to less than a few percent difference (Tsuchiya et al. 2005). We caution that although phase changes do not need to be considered, theoretical calculations are needed to compute an accurate EOS at high pressures (i.e., between 200 and  $10^4$  GPa) because in many cases an extrapolation of the BME or Vinet EOS fit will not do (see §3.3). For example, for some water ice planets with masses above  $10 M_{\oplus}$ , the effect of extrapolating the BME fit without considering a more accurate higher pressure EOS is considerable (Figure 7d).

At very high pressures the TFD EOS becomes valid. To understand the planet mass range where TFD effects are important, we show planet mass-radius relationships in the case of ignoring the TFD EOS in the dotted lines in Figure 7, i.e. in using only the extrapolated BME or Vinet fit.

#### 4.2.2. Temperature

Temperature has little effect on the radius of solid exoplanets. The reason is that the density of a solid changes by a relatively small amount under the influence of thermal pressure. At low pressures, the crystal lattice structure dominates the material's density and the thermal vibration contribution to the density is small in comparison. At high pressures, the close-packed nature of the atoms prevents any significant structural changes from thermal pressure contributions. Moreover, any change in average density of a planet of fixed composition results in a smaller change in the planet radius than the change in average density, because  $R_p \sim \bar{\rho}_p^{-1/3}$ .

Some authors have stated or shown with models that temperature is not important for deriving a planet's total mass and radius (see e.g., Valencia et al. 2006, 2007b; Fortney et al. 2007; Sotin et al. 2007, and references therein). In this subsection we go into detail to estimate the effect of temperature on density for the three main materials that we studied, iron, silicates, and water ice VII.

Heating planetary material adds a thermal contribution to the pressure term. In a first approximation one can assume that the thermal pressure is a linear function of temperature (e.g., Anderson & Goto 1989; Poirier 2000). The thermal contribution to the pressure,  $P_{th}$ , can be written as:

$$P_{th} = \int_0^T \left( \frac{\partial P}{\partial T} \right)_V dT = \int_0^T \alpha(T) K_0(T) dT. \quad (7)$$

Here  $\alpha(T)$  is the thermal expansivity and  $K_0(T)$  is the bulk modulus as before.

For most cases the term  $\alpha(T)K_0(T)$  is independent of volume above the Debye temperature  $\Theta_D$  (Anderson & Goto 1989). The thermal pressure term can then be written

$$P_{th} = \int_0^{\Theta_D} \alpha K_0 dT + \alpha K_0 (T - \Theta_D). \quad (8)$$

Note that the  $\Theta_D$  is around 700K for silicate- and Fe-bearing minerals.  $\Theta_D$  is significantly lower (300K) for water ice and significantly higher for carbon (2000K). Moreover, for Earth-bearing minerals Anderson & Goto (1989) find that  $P_{th}$  is linear in  $T$  down to much lower temperatures, and find that

$$P_{th} = \alpha K_0 (T - 300 \text{ K}). \quad (9)$$

For  $(\text{Mg,Fe})\text{SiO}_3$  we use  $\alpha K_0 = 0.00692$  GPa/K from Anderson & Masuda (1994). We note that, for our purposes,  $(\text{Mg,Fe})\text{SiO}_3$  is similar enough to  $\text{MgSiO}_3$  for estimating the thermal pressure.

For metals the thermal excitation of electrons must be taken into account by including a higher order term (Isaak & Anderson 2003, and references therein),

$$P_{th} = \alpha K_0 (T - 300 \text{ K}) + \frac{\partial \alpha K_0}{\partial T}_V (T - 300 \text{ K})^2. \quad (10)$$

We use values of  $\alpha K_0 = 0.00121$  GPa  $\text{K}^{-1}$  and  $(\partial \alpha K_0)/(\partial T)_V = 7.8 \times 10^{-7}$  GPa  $\text{K}^{-2}$  from Isaak & Anderson (2003).

For  $\text{H}_2\text{O}$  ice VII, we constructed  $P_{th}$  based on (P,V) isotherms according to the thermodynamic relations in equations (2) and (3) in Fei et al. (1993). This method uses a linear fit with  $T$  to  $\alpha(T)$  and a parameter  $\eta_1$  which describes the pressure effect on the measured volume at high temperature. We take the parameters from Frank et al. (2004).

Figure 12 shows  $P_{th}$  vs. temperature for Fe, H<sub>2</sub>O ice VII, and (Mg,Fe)SiO<sub>3</sub>.  $P_{th}$  increases more slowly at high pressure than at low pressure because at high pressure the thermal expansion becomes a constant; the atoms become tightly packed so that any thermal pressure has a decreasing contribution to the total pressure. Although water ice data is only available for ice VII to 50 GPa and  $\sim 800$  K (Frank et al. 2004), we expect it to show the same  $P_{th}$  trend with increasing temperature as other materials.

We can estimate the change in density caused by a thermal pressure. We computed  $\rho(T)$  corresponding to the total pressure  $P_{total} = P + P_{th}$  using the EOSs described in 3.3. Figures 12 to 13 show  $(P, \rho)$  isotherms for the main materials we studied.

For MgSiO<sub>3</sub>, the decrease in density due to thermal pressure is less than 4 percent over the temperature range 300 K to 6000 K and above 10 GPa where the material is solid (Figure 13a). Below 10 GPa the decrease in density is less than 2.5 percent for temperatures up to 1200 K (Figure 13b and for densities less than the zero-pressure 300 K density see Figure 7 in Anderson & Masuda (1994).)

Fe is known to have a higher thermal expansivity than MgSiO<sub>3</sub> and its density therefore decreases more than MgSiO<sub>3</sub> for the same temperature increase. The Fe density decrease is less than four percent for pressures above 100 GPa (Figure 14a). Earth’s Fe core is at pressures higher than 100 GPa (Dziewonski & Anderson 1981), and we expect the same for more massive differentiated planets with similar composition (see, e.g. Valencia et al. (2006)). We further note that as the planet’s Fe mass fraction increases, more of the planet’s mass is at higher pressures, making the material’s density change at low pressure in response to temperature less relevant. For example, Figure 11 shows that for a pure Fe planet with  $M_p > 0.1M_{\oplus}$ , 97 percent of the planet’s mass is above 1 GPa and for planets with  $M_p > 1M_{\oplus}$  97 percent of the planet’s mass is above 10 GPa.

Using available data to 50 GPa and 800 K (Frank et al. 2004), we find that H<sub>2</sub>O water ice VII density changes by less than a few percent throughout this pressure and temperature range (Figure 14b). We note that above approximately 1000 K water ice reaches an ionic fluid phase (Goncharov et al. 2005). Nevertheless, we emphasize that our water ice EOS (which includes phases VII, VIII, and X; see Table 2) agrees with recent Hugoniot shock data to within the experimental uncertainties. This recent data is from Lee et al. (2006) and ranges in pressure from 47 to 250 GPa and temperature from 2100 K all the way to 19,000 K. More work needs to be done to quantify the thermal pressure effects above 250 GPa and in the ionic phase, which is beyond the scope of this paper.

Our  $(P, \rho)$  isotherms in Figures 13 and 14 can be interpreted in light of the temperature-pressure profiles of planetary interiors. Earth, for example, has temperatures of approximately 1000 K at 50 GPa, 2000 K at 150 GPa and up to 6000 K at 350 GPa (Poirier 2000). Super-Earth interior models calculated in Valencia et al. (2006) shows that below 1 GPa the temperature is less than 1600 K, above 100 GPa the temperature is 2500 K, and the temperature is up to about 7000 K at hundreds of GPa. Isotherms for Neptune are expected to be about 2500 K at 20 GPa and to reach 7000 K at 600 GPa. The fact that high

temperatures are reached only at high pressures lessens the temperature effect because the fractional contribution of the thermal pressure to the total pressure decreases as the total pressure increases (Figure 12).

We argue that even for the short-period hot exoplanets—those in few day orbits whose surface temperatures could reach 1000 to 2000 K—the thermal pressure contribution to radius is still small. This statement is based on the argument that for solid planets above one to a few Earth masses (depending on composition) the fractional radius affected by such high temperatures is small.

Based on the above discussion of density decrease as a function of temperature we illustrate the effect of temperature on planet radius by the following example. Taking a case where the average density is overestimated by 3.5 percent in a uniform 300 K temperature models, the planet’s total radius would be underestimated by only 1.2 percent. This is due to the  $R_p \sim \bar{\rho}_p^{-1/3}$  scaling.

## 5. A GENERIC MASS-RADIUS RELATIONSHIP FOR SOLID EXOPLANETS

A glance at Figure 4 may suggest to the astute reader that the mass-radius relationships for a variety of planets all have a similar functional form, perhaps caused by some symmetry of the underlying equations. Indeed, there is such a symmetry, and a common functional form: a generic mass-radius relationship which we describe here. This generic mass-radius relationship is valid for planet masses up to about  $20 M_{\oplus}$ .

### 5.1. A Modified Polytopic Equation of State

Our generic mass-radius relationship is based on the similar forms of the EOSs of all solid materials we have considered. The zero-temperature or 300 K temperature EOSs for the solid materials we considered can be approximated by the function

$$\rho(P) = \rho_0 + cP^n. \quad (11)$$

Table 4 lists the best-fit parameters  $\rho_0$ ,  $c$ , and  $n$  for some materials over the range  $P < 10^{16}$  Pa. The density given by these approximate EOSs match the density given by the more detailed EOSs we used above to within 2 to 5% for the pressure ranges  $P < 5 \times 10^9$  and  $P > 3 \times 10^{13}$  Pa. At intermediate pressures, the discrepancy ranged from less than 1% to 12%.

The similarity of the EOSs of all solid materials stems from the the behavior of chemical bonds under pressure. At low pressures the chemical bonds of the material can withstand compression. Above some pressure, the energy imparted to the material breaks the chemical bonds and the material structure radically changes. The “crossover” pressure is roughly the material’s bulk modulus. For our simple analytic EOS, the bulk modulus is

$$K \approx \left(\frac{\rho_0}{c}\right)^{\frac{1}{n}}. \quad (12)$$

Our approximate EOS is a modified polytopic EOS. Polytopic EOSs are of the form  $P = K_p \rho^{1+1/m}$ , or  $\rho = (P/K_p)^{m/(m+1)}$ , where  $K_p$  is a constant and  $m$  is the polytopic index. Our approximate EOS fit differs from the polytopic EOS by the addition of the constant  $\rho_0$ ; it incorporates the approximate incompressibility of solids and liquids at low pressures.



## 5.2. Dimensionless Equations of Planetary Structure

The new generic EOS contains some dimensional quantities,  $\rho_0$  and  $c$ , that allow us to conveniently write equations (1) and (2) in dimensionless form. We rescale the variables  $P$ ,  $\rho$ ,  $m$ , and  $r$  as follows, where the subscript  $s$  refers to a scaled variable,

$$\rho_s = \frac{\rho}{\rho_0} \quad (13)$$

$$P_s = \frac{P}{P_1} \quad (14)$$

$$r_s = \frac{r}{r_1} \quad (15)$$

$$m_s = \frac{m}{m_1} \quad (16)$$

where

$$P_1 = \left(\frac{\rho_0}{c}\right)^{1/n} \quad (17)$$

$$r_1 = G^{-1/2} \rho_0^{(1/2n-1)} c^{-1/2n} \quad (18)$$

and

$$m_1 = r_1^3 \rho_0. \quad (19)$$

With this change of variables, the equations of planetary structure become: mass of a spherical shell

$$\frac{dm_s(r)}{dr_s} = 4\pi r_s^2 \rho_s(r_s); \quad (20)$$

hydrostatic equilibrium

$$\frac{dP_s(r_s)}{dr_s} = -\frac{\rho_s(r_s)m_s(r_s)}{r_s^2}; \quad (21)$$

and the EOS

$$\rho_s = 1 + P_s^n. \quad (22)$$

Figure 15 shows dimensionless mass-radius relationships derived by numerically solving the above equations the same way we solved the unscaled equations. It shows the total dimensionless planet mass,  $M_s$  as a function of the scaled planet radius,  $R_s$ , where  $R_s$  is defined by the outer boundary condition  $P(R_s) = 0$ . At  $R_s$  we also have  $M_s = m_s(R_s)$ . We generated the numerical mass-radius curves by solving the equations for a range of central pressure values of  $P_s$ .

The dimensionless mass-radius curves depend only on  $n$ . We plot curves for three values of  $n$ :  $n = 0.513$  ( $\text{H}_2\text{O}$ ),  $n = 0.528$  (Fe), and  $n = 0.544$  (silicate). These values of  $n$  span the range of behaviors of all the EOSs we studied. We also show solutions for the interior structure of homogeneous planets in Figure 16.

The solutions behave quite differently on either side of the line  $M_s = 1$ . For  $M_s < 1$ ,  $R_s$  strictly increases with  $M_s$ , and does not depend on  $n$ . For  $M_s > 1$ ,  $R_s$  depends strongly on  $n$  and does not necessarily strictly increase with  $M_s$ . This contrasting behavior arises because for  $M_s \ll 1$ , the EOS reduces to  $\rho_s = 1$ , and for for  $M_s \gg 1$ , the EOS reduces to the polytropic form  $\rho_s = P_s^n$ .

Table 4 lists some values of  $m_1$ ,  $r_1$ , and  $P_1$  for some EOSs based on the values of  $\rho_0$ ,  $n$ , and  $c$  listed in Table 3. Curiously, the scaling parameters  $m_1$  and  $r_1$  are somewhat similar for the polytropic-like mass-radius solutions for  $\text{H}_2\text{O}$  and Fe because these materials have similar ratios of  $K_0/\rho_0$ .

For  $M_s < 4$ , the dimensionless mass-radius relationship is approximately

$$\log_{10} R_s = k_1 + 1/3 \log_{10}(M_s) - k_2 M_s^{k_3}, \quad (23)$$

where  $k_1 = -0.20945$ ,  $k_2 = 0.0804$ , and  $k_3 = 0.394$ ; this approximation is good to 1% over this range. For  $M_s > 4$ , the scaled radius becomes a strong function of  $n$ . But We can use the analytic function in equation (23) to describe the dimensionless mass-radius relationships for scaled masses,  $M_s$ , up to  $\sim 40$  if we use the values of  $k_i$  for different materials listed in Table 4.

Equation (23) and the scaling parameters in Table 4 provide a convenient approximate summary of the results of this paper for homogeneous planets.

It may appear that the scaled mass-radius relationship is not useful for differentiated planets, since differentiated planets combine materials with different equations of state. We find, however, that even the radii of differentiated planets are well described by the functional form shown in Figure 15 for  $M_s \lesssim 4$  (i.e., up to where the scaled numerical solutions for different materials differ from each other).

This circumstance provides us with a convenient way to summarize our results for differentiated planets. To any differentiated planet model, we can assign an effective  $m_1$  and  $r_1$ . These effective scalings allow us to summarize *all* of our calculated mass-radius relationships using equation (23)—regardless of whether they were computed with the modified-polytropic EOS or our actual Vinet/BME and TFD EOSs. Table 4 lists some effective values of  $m_1$  and  $r_1$  for a few examples of differentiated planets. We calculated these numbers by comparing the mass-radius curves for differentiated planets (shown in Figure 4) to equation (23). To find the approximate mass-radius relationship for any given planet, look up  $m_1$  and  $r_1$  in Table 4 and plug these numbers into equation (23) using  $k_1 = -0.20945$ ,  $k_2 = 0.0804$ , and  $k_3 = 0.394$ .

The scaled variables help us to understand why the solid planet mass-radius relationships are very nearly the same for all materials we considered, for  $M_s \leq 1$ . We first recall that  $M_s = 1$  is defined as the mass so that the central, i.e. the maximum, pressure in the planet is  $P_s = 1$ . Next, for  $P_s \leq 1$ , i.e. everywhere in the planet for  $M_s \leq 1$ , the density (or the scaled density) never changes by more than 2.5 percent if a variation of  $n$  in the range of 0.513 to 0.549. Hence the radius (or the scaled radius) never changes by more than 0.85 percent (due to the  $R_p \sim \rho^{-1/3}$  scaling).

## 5.3. Analytic Treatment of the Dimensionless Equations

Here we will derive an approximate analytic solution to the dimensionless equations of planetary structure. The existence and form of the solution demonstrates why the mass-radius curves for various planets all look so similar. The good agreement between this approximate solution and our calculations gives us confidence in our results.

We first discuss a general analytic solution to equations (1) and (2), followed by an application to the dimensionless equations (20) and (21). For most equations of state, equations (1) and (2) cannot be solved analytically, even given the approximation of zero temperature. We can incorporate two ideas to allow new analytic progress. First, over a wide range of low pressures below a GPa, solids and liquids change their densities by a small amount—much

less than ten percent. This point enables us to assume an equation of state that encapsulates the idea of materials that are largely incompressible over a wide range of low pressures:

$$\rho(P) = \rho_0 + f(P). \quad (24)$$

We have shown in §5.1 that  $f(P) = cP^n$  is a good approximation. We further note, however, that in the range of low pressures we can assume  $f(P) \ll \rho_0$ .

The second point that enables an analytic treatment is that, when a planet is massive enough that it begins to compress under its own gravity, the compression is most acute at the planet's center. With these two ideas in mind, we can obtain an approximate solution to equations (1) and (2), and a mass-radius relationship for the case of a low-mass, slightly compressed planet.

To zeroth order,  $\rho(P)$  does not depend on  $P$ , so we can integrate equations (1) and (2) to find the zeroth order solutions:

$$m(r) = \frac{4}{3}\pi r^3 \rho_0, \quad (25)$$

$$P(r) \approx P_c - \frac{2}{3}\pi G r^2 \rho_0^2. \quad (26)$$

Here,

$$P_c = \frac{2}{3}\pi G R_p^2 \rho_0^2 = \frac{3G}{8\pi} \frac{M_p^2}{R_p^4}, \quad (27)$$

where  $M_p$  is the total mass of the planet, and  $R_p$  is the planet's radius.

Now we can use the zeroth order solution for  $P(r)$  to write equation (24) to 1st order in the term  $f(P(r))$ :

$$\rho(P) \approx \rho_0 + f(P(r) = P_c - \frac{2}{3}\pi G r^2 \rho_0^2). \quad (28)$$

Keeping in mind that the compression is most important in the center, we will expand this expression for  $\rho$  about  $r = 0$ , to get an expression for the density accurate to first order in  $f(P(r))$  and second order in  $r/R$ :

$$\rho(P_c) \approx \rho_0 + \left[ f(P_c) - \frac{2}{3}\pi G r^2 \rho_0^2 f'(P_c) \right]. \quad (29)$$

If the compressed region is confined to small  $r/R$ , then we can use this expression as an approximation for the pressure everywhere in the planet. We can then substitute this expression into equation (1) and integrate to get

$$m(r) \approx \frac{4}{3}\pi r^3 \left[ \rho(P_c) - \frac{2}{5}\pi G r^2 \rho_0^2 f'(P_c) \right]. \quad (30)$$

When we evaluate this equation at  $r = R_p$ , we find the desired mass-radius relationship

$$M_p = \frac{4}{3}\pi R^3 \left[ \rho(P_c) - \frac{2}{5}\pi G R_p^2 \rho_0^2 f'(P_c) \right]. \quad (31)$$

The mean density is

$$\bar{\rho} = \rho(P_c) - \frac{2}{5}\pi G R_p^2 \rho_0^2 f'(P_c). \quad (32)$$

We can see that  $\rho(P_c) > \bar{\rho} > \rho_0$ , i.e., the mean density is higher than the zero pressure density but lower than the density near  $r = 0$ . Also, for high  $P_c$  the radius will decrease (this is the case for  $f(P_c) = cP_c^n$ , the modified-polytropic form in equation (11)).

We can evaluate equation (32) to first order in  $f(P(r))$  using equation (27). In other words, the mean density of the planet is approximately

$$\bar{\rho} = \rho(P_c) - \frac{3}{5}f'(P_c)P_c, \quad (33)$$

where  $P_c$  is given in equation (27).

We now apply the above analytic equations equations (26)–(33) to our dimensionless equations. We begin by considering our scaled equation of state as

$$\rho_s(P_s) = 1 + P_s^n. \quad (34)$$

We proceed under the assumption that  $P_s \ll 1$  and therefore  $P_s^n \ll 1$ . For the dimensionless equations we find: the scaled pressure

$$P_s(r_s) \approx P_{s,c} - \frac{2}{3}\pi r_s^2 \quad (35)$$

where

$$P_{s,c} = \frac{2}{3}\pi R_s^2; \quad (36)$$

the scaled central density

$$\rho_s(P_{s,c}) \approx 1 + \left( P_{s,c}^n - \frac{2}{3}\pi r_s^2 n P_{s,c}^{n-1} \right); \quad (37)$$

the scaled mass

$$m_s(r_s) \approx \frac{4}{3}\pi r_s^3 \left[ 1 + P_{s,c}^n - \frac{2}{5}\pi n r_s^2 P_{s,c}^{n-1} \right]; \quad (38)$$

the desired mass-radius relationship

$$M_s \approx \frac{4}{3}\pi R_s^3 \left[ 1 + \left( 1 - \frac{3}{5}n \right) \left( \frac{2}{3}\pi R_s^2 \right)^n \right]; \quad (39)$$

and the average density

$$\bar{\rho}_s = 1 + \left( 1 - \frac{3}{5}n \right) \left( \frac{2}{3}\pi R_s^2 \right)^n. \quad (40)$$

Because we chose  $P_s \ll 1$  for this analytic derivation, we know exactly over what range of parameters these approximations are valid. They apply where  $P_s \ll 1$ , which is also where  $R_s \ll 1$  and  $M_s \ll 1$ . The correction term in equations (39) and (40),  $\left[ \left( 1 - \frac{3}{5}n \right) \left( \frac{2}{3}\pi R_s^2 \right)^n \right] \ll 1$ . The  $R_s \ll 1$  limit therefore shows why the scaled mass-radius relation depends very weakly on composition: the correction term in equation (39) is small.

If we consider the scaled mass-radius relationship equation (39) slightly beyond where it is formally valid ( $R_s < 1$  instead of  $R_s \ll 1$ ), we find that it is still a reasonable approximation. While the scaled mass-radius relationship equation (39) is good to within 1% at  $M_s = 0.245$  it is good to within 5% at  $M_s = 0.36$  (compared to the numerical solution to the scaled equations). Even at  $R_s \approx 1$ , the correction term is never larger than  $(1 - \frac{3}{5}n)(\frac{2}{3}\pi)^n$ . Since  $n$  ranges typically from 0.5–0.6, this maximum value for the correction term ranges from about 0.997 to 1.013. In other words, even for  $R_s \approx 1$ , the correction term in equation (39) varies over only a range of about 0.02 as a function of planet chemistry.

Figure 15 compares this analytic mass-radius approximation to the full numerical solution of the scaled equations, justifying that our calculations are correct.

## 6. DISCUSSION

### 6.1. *Exoplanet Mass and Radius Observational Uncertainties*

We now discuss the observational uncertainties on the mass and radius of transiting exoplanets. We adopt a conservative range for planet mass and radius fractional uncertainty of 2–10%. The 10% limit is the uncertainty range for typical exoplanet detections, arising from measurement uncertainty due to the data quality. Once discovered, most exoplanets of interest will be followed up with larger telescopes and/or more observations to refine the planet mass and radius beyond that determined from the observational discovery. If measurement uncertainty is not a dominant factor for planet mass and radius uncertainty, then the stellar mass and radius uncertainty are. This is because the exoplanet mass and radius are derived from quantities that involve planet-star mass or radius ratios. Note that assuming the stellar noise to be small, the measurement uncertainty and stellar mass or radius uncertainty add in quadrature.

Our estimate of the 2% planet mass and radius uncertainty is based on an optimistic assessment of the 2% stellar mass and radius uncertainty likely to be possible for millions of stars in the future. This kind of high-precision measurement will be enabled with accurate distances and precise stellar fluxes by the GAIA space mission (ESA; launch date 2013). In practice the radius can be inferred directly from the stellar fluxes and distances; in principle a precise radius is limited by the correction from a measured stellar flux to the star’s bolometric flux (D. Sasselov, 2006 private communication). In contrast to our 2% best case scenario, current typical stellar mass and radius uncertainties are on the order of 5–10% (Ford et al. 1999; Cody & Sasselov 2002; Fischer & Valenti 2005). These stellar masses and radii are derived from interior and evolution model fits to observed stellar spectra. Sozzetti et al. (2007) show that a more precise stellar radius (and hence planet radius) can be derived using stellar evolution models in the  $a/R_*$  vs.  $T_{eff}$  parameter space instead of in the usual  $\log g$  vs.  $T_{eff}$  parameter space. This is partly because  $a/R_*$  (a measure of stellar density) can be determined with high precision from the planet transit light curve for planet’s with zero orbital eccentricity (Seager & Mallén-Ornelas 2003). Provided the photometry is good enough, few percent uncertainty in star and planet radii may become routine. We note that a different technique, interferometry, can measure stellar radii directly, but the current uncertainties are much higher than 2% and the technique is limited to a small number of nearby stars.

The mass determination of low-mass planets by ground-based radial velocity techniques require hundreds of observations. Mass determination for many exoplanets may therefore be inhibited (Lovis et al. 2006) until a number of dedicated ground-based telescopes are available. Given such limitations of telescope time and current technology, the optimistic future exoplanet mass uncertainty range is likely closer to 5–10% for the low-mass solid planets of interest ( $< 20M_{\oplus}$ ). With current technology and due to the faintness of the host stars, many low-mass exoplanets discovered from transit surveys (e.g., COROT or Ke-

pler) will not have measured masses at all. As an example of what it would take to detect an Earth-mass planet in a 50-day orbit about one of the brightest sun-like stars: one eight meter diameter telescope dedicated to five bright stars monitored over five years (R. P. Butler 2006, private communication). Earth-mass planets more distant from their host stars, such as Earth-like orbits about sun-like stars cannot be detected with any current technology.

### 6.2. *Possible Exoplanet Compositional Distinctions*

Given the observational uncertainties, what compositional distinctions among exoplanets can we make? With an upper limit of 20% on the planet mass uncertainty we will be able to say robustly that the planet is predominantly composed of solids or if it instead has a significant gas envelope as do Uranus and Neptune.

The following discussion assumes we can ascertain that the planet has no substantial atmosphere or envelope that would contribute to the planet radius (c.f. Adams et al., in prep).

With a 10% uncertainty we may be able to comment on the presence of a large amount of water or iron—if the planet fortuitously has a very low density or a very high density within the radius range for solid planets.

A  $\sim 5\%$  uncertainty will allow us to distinguish among planets composed predominantly of water-ice, predominantly of silicates, and predominantly of iron (sections 4.1.1 and 4.1.2). These planets are relatively well separated on the mass-radius diagram (Figure 4). Their separation is primarily due to the low density of water ice, the intermediate density of silicates, and the high density of Fe. Even with 5% exoplanet mass and radius uncertainties, it is not possible to identify the detailed composition such as the fraction of different material in the core and differentiated layers.

Identification of water planets is possible with  $\sim 5\%$  planet mass and radius uncertainty if the planet has more than 25% water ice by mass and plausible iron-to-silicate ratios. With the same  $\sim 5\%$  uncertainty, water planets with 50% water by mass with any iron-to-silicate ratio can be identified. Water exoplanets should exist; in our own solar system Jupiter’s satellite Ganymede is 45% water ice by mass. Water ice planets should be the easiest of the solid exoplanets to detect observationally because of their large radius for a given planet mass—they could be as large as  $3R_{\oplus}$  for  $M_p = 20M_{\oplus}$ . We note that Valencia et al. (2007b) came to the same conclusion for the one planet mass they explored water compositions of, the  $7.5 M_{\oplus}$  Gl 876d. A detection of a low-density water-ice planet orbiting far interior to the expected snow line in the disk where the planet formed would be strong evidence for planet migration.

With 2% uncertainty in planet mass and radius we would be able to determine not only the basic composition of any iron/silicate/water planet, but constrain the relative fraction of each material. However, even with 2% uncertainty in planet mass and radius many degeneracies in planet composition remain for a planet of the same mass and radius. For example, carbon planets with silicate mantles and iron cores are indistinguishable from silicate planets with small iron cores, or with planets that have a small ( $\sim 10\%$  by mass) fraction of water on top

of a silicate mantle and iron core. As a second example, planets with deep water oceans (even 100 km deep) on any kind of planet are not identifiable with even 2% fractional uncertainty in the radius. This is because a liquid water ocean contributes only a small amount to the overall planet radius compared to a pure water ice layer. For a third example, see Figure 6d and the accompanying discussion. See also Valencia et al. (2007a) for a detailed discussion of degeneracies in composition for iron-silicate-water planets of 1–10  $M_{\oplus}$ .

Observational uncertainties in planet mass and radius are unlikely to be better than a few percent in the next decade. We therefore argue that detailed exoplanet interior models are not needed to infer exoplanet bulk composition. The analytical form derived in this paper (equation (23)), with scaling relations provided from model curves (e.g., in Table 4), should be sufficient for the near future.

Exoplanet atmosphere measurements may inform us about the planet interior, removing some of the degeneracies in a given solid exoplanet mass and radius relationship. Therefore, despite our conclusions that detailed interior planet models are not needed to determine exoplanet bulk composition, we point out that detailed interior models are required to understand planetary atmospheres. In turn, observations of exoplanet atmospheres may help us infer more about the exoplanet interior composition. Atmosphere measurements will also help us to identify interesting features on planets, such as the presence of a deep liquid ocean. A saturated water vapor atmosphere would be a better indicator than an exoplanet mass and radius, considering we cannot identify deep water oceans with mass-radius relationships.

## 7. SUMMARY AND CONCLUSIONS

We have modeled cold solid planets of a variety of compositions including iron, silicates, water, and carbon compounds. The main conclusions of this work are:

1. All solid planets approximately follow the scaled mass-radius relationship  $\log_{10} R_s = k_1 + 1/3 \log_{10}(M_s) - k_2 M_s^{k_3}$  for up to  $M_p \simeq 4M_s$ . This relationship can be scaled to physical units by the values  $m_1$  and  $r_1$  given in Table 4. The corresponding planet mass, in physical units, to which the above mass-radius equation is valid ranges from  $M = 17M_{\oplus}$  to  $M_p = 40M_{\oplus}$ , depending on the material (see the  $m_1$  values in Table 4.)

2. There is no simple power law for the mass-radius relation; the mass-radius curve slope changes even within a relatively narrow mass range.

3. We can use the same formalism described in the above equation to summarize the mass-radius relationships we computed for differentiated planets, using the scaling parameters listed in Table 4. Given the uncertainties in the equations of state and the best expected future observations, this simple, handy approximation supplies enough detail and accuracy to interpret any forecasted observations.

4. Highly detailed interior planet models are not needed to infer a solid exoplanet’s bulk composition from its mass and radius. This is because the temperature structure and phase changes have little impact on the total planet mass and radius.

- a. Low-pressure phase changes (at  $< 10$  GPa) are not important for a planet’s radius because for plausible planet compositions most of the mass is at high pressure. For example, 97% of the planet’s mass is at high pressures ( $> 3$  GPa). For high pressure phase changes we expect the associated correction to the EOS (and hence derived planet radii) to be small because at high pressure the importance of chemical bonding patterns to the EOS drops.

- b. Temperature can be approximated as a thermal pressure term. This thermal pressure causes a decrease in density of on order three percent or less at relevant temperatures and pressures. A change in average density of a planet translates into a smaller change in the planet radius, because  $R_p \sim \bar{\rho}_p^{-1/3}$ . Conceptually, At low pressures ( $\lesssim 10$  GPa) in the outer planetary layers, the crystal lattice structure dominates the material’s density and the thermal vibration contribution to the density are small in comparison. At high pressures the thermal pressure contribution to the EOS is small because close-packed nature of the materials prevents structural changes from thermal pressure contributions.

5. We identified several interesting properties of exoplanets.

- a. Planets are not likely to be found that have radii smaller than a pure Fe planet. Fe is the most dense element out of which planets are expected to form. While not a new conclusion, this point is useful to keep in mind for designing and interpreting radius observations of exoplanets.

- b. Planets above the  $H_2O$  curve must have a significant H/He envelope. We can therefore easily distinguish between exoplanets with significant H/He envelopes and those without, as is the case for GJ 436b. We therefore define a “super Earth” to be a solid planet with no significant gas envelope, regardless of its mass.

- c. Because of their unique position on the mass-radius diagram,  $H_2O$  planets with more than 25% water ice by mass can be identified with approximately 5% fractional uncertainty in  $M_p$  and  $R_p$ . (A similar conclusion was also found by Valencia et al. (2007b); that if the 7.5  $M_{\oplus}$  planet they modeled has a large water content it would be identified by a large radius.) Discovering a water planet orbiting at a small semi-major axis would serve as strong evidence for planet migration, since presumably water planets form more efficiently far from their host stars, beyond the ice line. This point is valid provided the planet is not a carbon planet and provided there is no substantial contribution to the planet radius from an atmosphere or envelope.

- d. Even with planet mass and radius measurement uncertainties better than 1%, planets of different interior composition can have the same total mass and radius. In other words, different mass fractions of iron cores, silicate mantles, and water outer layers can have the same total radius for a planet of the same mass.

- e. Carbon planets, if they exist, have mass-radius relationships that overlap with mass-radius relationships of non-carbon planets (i.e., water and silicate planets). This is because the zero-pressure density of graphite is similar to that of  $H_2O$  and the zero-pressure density of SiC is similar to that of  $MgSiO_3$ . Exoplanet atmospheres of transiting exoplanets will have to be observed and studied to distinguish between carbon planets and water/silicate

planets.

6. We conclude that, while detailed interior structure models are needed to understand the atmosphere formation and evolution, detailed interior structure models are not needed to infer bulk composition from exoplanet mass and radius measurements.

We dedicate this study of mass-radius relationships to the memory of our co-author Cathy Hier-Majumder. It is with great sadness that we acknowledge her untimely death. We thank Rus Hemley, Y. Fei, and Dan

Shim for extremely useful discussions about high pressure physics and equations of state. We thank Mercedes Lopez-Morales, Dimitar Sasselov, Jim Elliot for useful discussions about observational uncertainties. We thank Diana Valencia for providing a more detailed version of Figure 4 in Valencia et al. (2006), as well as for interesting discussions about unpublished work. This work was supported by the Carnegie Institution of Washington, the NASA Astrobiology Institute, and the Massachusetts Institute of Technology.

## REFERENCES

- Ahrens, T. J. 2000, *Mineral Physics and Crystallography: A Handbook of Physical Constants* (Washington, DC: American Geophysical Union)
- Aleksandrov, I. V., Gocharov, A. F., Stishov, S. M., & Yakovenko, E. V. 1989, *JETP Lett*, 50, 127
- Anderson, O. L., Dubrovinsky, L., Saxena, S. K., & LeBihan, T. 2001, *Geophys. Res. Lett.*, 28, 399
- Anderson, O. L. & Goto, T. 1989, *Physics of the Earth and Planetary Interiors*, 55, 241
- Anderson, O. L. & Masuda, K. 1994, *Physics of the Earth and Planetary Interiors*, 85, 227
- Beaulieu, J.-P., Bennett, D. P., Fouqué, P., Williams, A., Dominik, M., Jorgensen, U. G., Kubas, D., Cassan, A., Coutures, C., Greenhill, J., Hill, K., Menzies, J., Sackett, P. D., Albrow, M., Brilliant, S., Caldwell, J. A. R., Calitz, J. J., Cook, K. H., Corrales, E., Desort, M., Dieters, S., Dominis, D., Donatowicz, J., Hoffman, M., Kane, S., Marquette, J.-B., Martin, R., Meintjes, P., Pollard, K., Sahu, K., Vinter, C., Wambsganss, J., Woller, K., Horne, K., Steele, I., Bramich, D. M., Burgdorf, M., Snodgrass, C., Bode, M., Udalski, A., Szymański, M. K., Kubiak, M., Więckowski, T., Pietrzyński, G., Soszyński, I., Szewczyk, O., Wyrzykowski, L., Paczyński, B., Abe, F., Bond, I. A., Britton, T. R., Gilmore, A. C., Hearnshaw, J. B., Itow, Y., Kamiya, K., Kilmartin, P. M., Korpela, A. V., Masuda, K., Matsubara, Y., Motomura, M., Muraki, Y., Nakamura, S., Okada, C., Ohnishi, K., Rattenbury, N. J., Sako, T., Sato, S., Sasaki, M., Sekiguchi, T., Sullivan, D. J., Tristram, P. J., Yock, P. C. M., & Yoshioka, T. 2006, *Nature*, 439, 437
- Birch, F. 1947, *Physical Review*, 71, 809
- Bonfils, X., Forveille, T., Delfosse, X., Udry, S., Mayor, M., Perrier, C., Bouchy, F., Pepe, F., Queloz, D., & Bertaux, J.-L. 2005, *A&A*, 443, L15
- Bonfils, X., Mayor, M., Delfosse, X., Forveille, T., Gillon, M., Perrier, C., Udry, S., Bouchy, F., Lovis, C., Pepe, F., Queloz, D., Santos, N. C., & Bertaux, J. 2007, *ArXiv e-prints*, 704
- Butler, R. P., Vogt, S. S., Marcy, G. W., Fischer, D. A., Wright, J. T., Henry, G. W., Laughlin, G., & Lissauer, J. J. 2004, *ApJ*, 617, 580
- Cameron, A. G. W., Benz, W., Fegley, B. J., & Slattery, W. L. The strange density of Mercury - Theoretical considerations (Mercury, University of Arizona Press), 692–708
- Chandrasekhar, S. 1939, *An introduction to the study of stellar structure* (Chicago, Ill., The University of Chicago press [1939])
- Cody, A. M. & Sasselov, D. D. 2002, *ApJ*, 569, 451
- Duffy, T. S., Hemley, R. J., & Mao, H.-K. 1995, *Physical Review Letters*, 74, 1371
- Dziewonski, A. M. & Anderson, D. L. 1981, *Phys. Earth Planet. Interiors*, 25, 297
- Ehrenreich, D., Lecavelier des Etangs, A., Beaulieu, J.-P., & Grasset, O. 2006, *ApJ*, 651, 535
- Eliezer, S., Ghatak, A., & Hora, H. 2002, *Fundamentals of Equations of State* (London: World Scientific Publishers Co.)
- Fei, Y., Mao, H.-K., & Hemley, R. J. 1993, *J. Chem. Phys.*, 99, 5369
- Fischer, D. A. & Valenti, J. 2005, *ApJ*, 622, 1102
- Ford, E. B., Rasio, F. A., & Sills, A. 1999, *ApJ*, 514, 411
- Fortney, J. J., Marley, M. S., & Barnes, J. W. 2007, *ApJ*, 659, 1661
- Frank, M. R., Fei, Y., & Hu, J. 2004, *Geochim. Cosmochim. Acta*, 68, 2781
- Gaidos, E. J. 2000, *Icarus*, 145, 637
- Gillon, M., Pont, F., Demory, B., Mallmann, F., Mayor, M., Mazeh, T., Queloz, D., Shporer, A., Udry, S., & Vuissoz, C. 2007, *ArXiv e-prints*, 705
- Goncharov, A. F., Goldman, N., Fried, L. E., Crowhurst, J. C., Kuo, I.-F. W., Mundy, C. J., & Zaug, J. M. 2005, *Physical Review Letters*, 94, 125508
- Gould, A., Udalski, A., An, D., Bennett, D. P., Zhou, A.-Y., Dong, S., Rattenbury, N. J., Gaudi, B. S., Yock, P. C. M., Bond, I. A., Christie, G. W., Horne, K., Anderson, J., Stanek, K. Z., DePoy, D. L., Han, C., McCormick, J., Park, B.-G., Pogge, R. W., Poindexter, S. D., Soszyński, I., Szymański, M. K., Kubiak, M., Pietrzyński, G., Szewczyk, O., Wyrzykowski, L., Ulaczyk, K., Paczyński, B., Bramich, D. M., Snodgrass, C., Steele, I. A., Burgdorf, M. J., Bode, M. F., Botzler, C. S., Mao, S., & Swaving, S. C. 2006, *ApJ*, 644, L37
- Halliday, D., Resnick, R., & Walker, J. 2003, *Fundamentals of Physics* (Fundamentals of Physics, by David Halliday, Robert Resnick, Jearl Walker, pp. . ISBN 0-471-44730-7. Wiley-VCH , January 2003.)
- Hanfland, M., Beister, H., & Syassen, K. 1989, *Phys. Rev. B*, 39, 12598
- Hemley, R. J., Jephcoat, A. P., Mao, H. K., S., Z. C., W., F. L., & Cox, D. E. 1987, *Nature*, 330, 737
- Hubbard, W. B. 1984, *Planetary interiors* (New York, Van Nostrand Reinhold Co., 1984, 343 p.), H83+
- Isaak, D. G. & Anderson, O. L. 2003, *Physica B Condensed Matter*, 328, 345
- Karki, B. B., Wentzcovitch, R. M., de Gironcoli, S., & Baroni, S. 2000, *Phys. Rev. B*, 62, 14750
- King, H. E. & Prewitt, C. T. 1989, *Acta Cryst.*, 38, 1887
- Knittle, E. & Jeanloz, R. 1987, *Science*, 235, 668
- Kresse, G. & Furthmüller, J. 1996, *Journal of Comput. Mater. Sci.*, 6, 15
- Kuchner, M. & Seager, S. 2006, *astro-ph/0504214*
- Kuchner, M. J. 2003, *ApJ*, 596, L105
- Lee, K. K. M., Benedetti, L. R., Jeanloz, R., Celliers, P. M., Eggert, J. H., Hicks, D. G., Moon, S. J., MacKinnon, A., da Silva, L. B., Bradley, D. K., Unites, W., Collins, G. W., Henry, E., Koenig, M., Benuzzi-Mounaix, A., Pasley, J., & Neely, D. 2006, *J. Chem. Phys.*, 125, 4701
- Léger, A., Selsis, F., Sotin, C., Guillot, T., Despois, D., Mawet, D., Ollivier, M., Labèque, A., Valette, C., Brachet, F., Chazelas, B., & Lammer, H. 2004, *Icarus*, 169, 499
- Lewis, J. S. 1974, *Science*, 186, 440
- Livio, M., Pringle, J. E., & Saffer, R. A. 1992, *MNRAS*, 257, 15P
- Lodders, K. & Fegley, Jr., B. 1997, in *American Institute of Physics Conference Series*, ed. T. J. Bernatowicz & E. Zinner, 391–+
- Lovis, C., Mayor, M., Pepe, F., Alibert, Y., Benz, W., Bouchy, F., Correia, A. C. M., Laskar, J., Mordasini, C., Queloz, D., Santos, N. C., Udry, S., Bertaux, J.-L., & Sivan, J.-P. 2006, *Nature*, 441, 305
- McArthur, B. E., Endl, M., Cochran, W. D., Benedict, G. F., Fischer, D. A., Marcy, G. W., Butler, R. P., Naef, D., Mayor, M., Queloz, D., Udry, S., & Harrison, T. E. 2004, *ApJ*, 614, L81
- Melo, C., Santos, N. C., Gieren, W., Pietrzyński, G., Ruiz, M. T., Sousa, S. G., Bouchy, F., Lovis, C., Mayor, M., Pepe, F., Queloz, D., da Silva, R., & Udry, S. 2007, *A&A*, 467, 721
- Murakami, M., Hirose, K., Kawamura, K., Sata, N., & Ohishi, Y. 2004, *Science*, 304, 855
- Nellis, W. J., Ree, F. H., van Thiel, M., & Mitchell, A. C. 1981, *J. Chem. Phys.*, 75, 3055
- Olinger, B. *Compression Studies of Forsterite (Mg<sub>2</sub>SiO<sub>4</sub>) and Enstatite (MgSiO<sub>3</sub>) (High Pressure Physics Research: Applications in Geophysics)*, 325–334
- Petrenko, V. F. & Whitworth, R. W. 1999, *Physics of Ice* (Oxford: Oxford University Press)
- Podsiadlowski, P., Han, Z., & Rappaport, S. 2003, *MNRAS*, 340, 1214
- Poirier, J.-P. 2000, *Introduction to the Physics of the Earth's Interior* (Cambridge, UK: Cambridge University Press)

- Rivera, E. J., Lissauer, J. J., Butler, R. P., Marcy, G. W., Vogt, S. S., Fischer, D. A., Brown, T. M., Laughlin, G., & Henry, G. W. 2005, *ApJ*, 634, 625
- Roberge, A., Feldman, P. D., Weinberger, A. J., Deleuil, M., & Bouret, J.-C. 2006, *Nature*, 441, 724
- Salpeter, E. E. & Zapolsky, H. S. 1967, *Physical Review*, 158, 876
- Santos, N. C., Bouchy, F., Mayor, M., Pepe, F., Queloz, D., Udry, S., Lovis, C., Bazot, M., Benz, W., Bertaux, J.-L., Lo Curto, G., Delfosse, X., Mordasini, C., Naef, D., Sivan, J.-P., & Vauclair, S. 2004, *A&A*, 426, L19
- Sato, B., Fischer, D. A., Henry, G. W., Laughlin, G., Butler, R. P., Marcy, G. W., Vogt, S. S., Bodenheimer, P., Ida, S., Toyota, E., Wolf, A., Valenti, J. A., Boyd, L. J., Johnson, J. A., Wright, J. T., Ammons, M., Robinson, S., Strader, J., McCarthy, C., Tah, K. L., & Minniti, D. 2005, *ApJ*, 633, 465
- Schubert, G., Anderson, J. D., Spohn, T., & McKinnon, W. B. Interior composition, structure and dynamics of the Galilean satellites (Jupiter. The Planet, Satellites and Magnetosphere), 281–306
- Seager, S. & Mallén-Ornelas, G. 2003, *ApJ*, 585, 1038
- Selsis, F., Chazelas, B., Borde, P., Ollivier, M., Brachet, F., Decaudin, M., Bouchy, F., Ehrenreich, D., Griessmeier, J. ., Lammer, H., Sotin, C., Grasset, O., Moutou, C., Barge, P., Deleuil, M., Mawet, D., Despois, D., Kasting, J. F., & Leger, A. 2007, *ArXiv Astrophysics e-prints*
- Sotin, C., Grasset, O., & Mocquet, A. 2007, *Icarus* in press
- Sozzetti, A., Torres, G., Charbonneau, D., Latham, D. W., Holman, M. J., Winn, J. N., Laird, J. B., & O'Donovan, F. T. 2007, *ArXiv e-prints*, 704
- Stevenson, D. J. 1982, *Planet. Space Sci.*, 30, 755
- Takahashi, Y. X. & Spain, I. L. 1989, *Phys. Rev. B*, 40, 993
- Tsuchiya, J., Tsuchiya, T., & Wentzcovitch, R. M. 2005, *Journal of Geophysical Research (Solid Earth)*, 110, 2204
- Udry, S., Bonfils, X., Delfosse, X., Forveille, T., Mayor, M., Perrier, C., Bouchy, F., Lovis, C., Pepe, F., Queloz, D., & Bertaux, J. . 2007, *ArXiv e-prints*, 704
- Udry, S., Mayor, M., Benz, W., Bertaux, J.-L., Bouchy, F., Lovis, C., Mordasini, C., Pepe, F., Queloz, D., & Sivan, J.-P. 2006, *A&A*, 447, 361
- Valencia, D., O'Connell, R. J., & Sasselov, D. 2006, *Icarus*, 181, 545
- Valencia, D., Sasselov, D. D., & O'Connell, R. J. 2007a, *ArXiv e-prints*, 704
- . 2007b, *ApJ*, 656, 545
- Vinet, P., Ferrante, J., Rose, J. H., & Smith, J. R. 1987, *J. Geophys. Res.*, 92, 9319
- Vinet, P., Rose, J. H., Ferrante, J., & Smith, J. R. 1989, *Journal of the Physics of Condensed Matter*, 1, 1941
- Vogt, S. S., Butler, R. P., Marcy, G. W., Fischer, D. A., Henry, G. W., Laughlin, G., Wright, J. T., & Johnson, J. A. 2005, *ApJ*, 632, 638
- Wolszczan, A. & Frail, D. A. 1992, *Nature*, 355, 145
- Wood, J. A. & Hashimoto, A. 1993, *Geochim. Cosmochim. Acta*, 57, 2377
- Zapolsky, H. S. & Salpeter, E. E. 1969, *ApJ*, 158, 809

Atom or Compound	$K_0$ (GPa)	$K'_0$	$\rho_0$ (Mg m $^{-3}$ )	Fit	$\log_{10}P_{V/T}$ (GPa)	Ref.
C (graphite)	33.8 $\pm$ 3	8.9 $\pm$ 1.0	2.25	BME	11.75	1,2
Fe ( $\alpha$ )	162.5 $\pm$ 5	5.5 $\pm$ 0.8	7.86	BME	–	1,3
Fe ( $\varepsilon$ )	156.2 $\pm$ 1.8	6.08 $\pm$ 0.12	8.30	V	13.32	4
FeS	35 $\pm$ 4	5 $\pm$ 2	4.77	BME	13.23	1,5
H $_2$ O (ice VII)	23.7 $\pm$ 0.9	4.15 $\pm$ 0.07	1.46	BME	–	6
H $_2$ O (liquid) <sup>a</sup>	2.28	–	–	–	–	7
MgO	177.0 $\pm$ 4	4.0 $\pm$ 0.1	3.56	BME	12.8	8
MgSiO $_3$ (en)	125	5 <sup>b</sup>	3.22	BME	–	1,9
MgSiO $_3$ (pv)	247 $\pm$ 4	3.97 <sup>c</sup>	4.10	BME4	13.13	10
(Mg $_{0.88}$ ,Fe $_{0.12}$ )SiO $_3$ (pv)	266 $\pm$ 6	3.9 $\pm$ 0.04	4.26	BME	12.74	1,11
SiC	227 $\pm$ 3	4.1 $\pm$ 0.1	3.22	BME	11.4	1,12

TABLE 1

PARAMETERS FOR THE VINET (V) OR BIRCH-MURNAGHAM (BME) EOS FITS. REFERENCES: (1) AHRENS (2000), (2) HANFLAND ET AL. (1989); (3) TAKAHASHI & SPAIN (1989); (4) ANDERSON ET AL. (2001); (5) KING & PREWITT (1989) (6) HEMLEY ET AL. (1987); (7) HALLIDAY ET AL. (2003); (8) DUFFY ET AL. (1995); (9) OLINGER (1977); (10) KARKI ET AL. (2000); (11) KNITTLE & JEANLOZ (1987); (12) ALEXSANDROV ET AL. (1989). A) SEAWATER AT 12 $^\circ$ K. B)  $K'_0$  VALUES ARE ASSUMED. C) A FOURTH ORDER BME FIT WAS USED WITH  $K''_0 = -0.016/\text{GPa}$ .

$V$ (cm $^3$ /mol)	$\rho$ (kg m $^{-3}$ )	P (GPa)
10.998300	1.636617	2.320
10.429585	1.725860	4.155
9.880818	1.821712	6.664
9.351623	1.924800	9.823
8.350443	2.155574	18.791
7.878082	2.284820	25.361
7.423411	2.424761	33.744
6.986806	2.576285	44.314
6.567891	2.740606	56.970
6.165913	2.919275	74.188
5.780497	3.113919	94.406
5.411641	3.326163	126.815
5.164734	3.485175	155.924
4.654734	3.867031	240.696
4.195170	4.290649	351.114
3.780772	4.760933	498.660
3.407399	5.282621	691.938
3.070912	5.861450	937.585
2.767547	6.503954	1260.182
2.494293	7.216474	1673.049
2.248138	8.006625	2188.301
2.026072	8.884186	2853.712
1.825836	9.858497	3691.387
1.645548	10.938603	4737.211
1.483327	12.134882	6040.611
1.336538	13.467635	7686.171

TABLE 2

DENSITY FUNCTIONAL THEORY (DFT) EOS FOR WATER ICE VIII AND X. DFT PREDICTS A GRADUAL TRANSITION BETWEEN THE TWO PHASES.

Material	$\rho_0$ [kg m <sup>-3</sup> ]	$c$ [kg m <sup>-3</sup> Pa <sup>-n</sup> ]	$n$
Fe( $\alpha$ )	8300.00	0.00349	0.528
MgSiO <sub>3</sub> (perovskite)	4100.00	0.00161	0.541
(Mg,Fe)SiO <sub>3</sub>	4260.00	0.00127	0.549
H <sub>2</sub> O	1460.00	0.00311	0.513
C (graphite)	2250.00	0.00350	0.514
SiC	3220.00	0.00172	0.537

TABLE 3

FITS TO THE MERGED VINET/BME AND TFD EOS OF THE FORM  $\rho(P) = \rho_0 + cP^n$ . THESE FITS ARE VALID FOR THE PRESSURE RANGE  $P < 10^{16}$  PA.



Material	$m_1 [M_\oplus]$	$r_1 [R_\oplus]$	$P_1 [\text{GPa}]$	$k_1$	$k_2$	$k_3$
Fe( $\alpha$ ) [modified-polytropic EOS]	5.80	2.52	1192	-0.209490	0.0804	0.394
MgSiO <sub>3</sub> (perovskite) [modified-polytropic EOS]	10.55	3.90	693	-0.209594	0.0799	0.413
H <sub>2</sub> O (ice) [modified-polytropic EOS]	5.52	4.43	114	-0.209396	0.0807	0.375
Fe( $\alpha$ )	4.34	2.23				
MgSiO <sub>3</sub> (perovskite)	7.38	3.58				
H <sub>2</sub> O (ice)	8.16	4.73				
Fe(0.675)/MgSiO <sub>3</sub> (0.325)	6.41	3.19				
Fe(0.3)/MgSiO <sub>3</sub> (0.7)	6.41	2.84				
Fe(0.225)/MgSiO <sub>3</sub> (0.525)/H <sub>2</sub> O(0.25)	6.41	3.63				
Fe(0.065)/MgSiO <sub>3</sub> (0.485)/H <sub>2</sub> O(0.45)	6.88	4.02				
Fe(0.03)/MgSiO <sub>3</sub> (0.22)/H <sub>2</sub> O(0.75)	7.63	4.42				

TABLE 4

CONVERSION FACTORS FOR THE SCALING RELATIONSHIPS FOR EQUATION (23). THE CONVERSION FACTORS GIVE THE PHYSICAL VALUES FROM THE SCALED PARAMETERS MASS, RADIUS, PRESSURE, AND DENSITY. SEE EQUATIONS (13) THROUGH (16). THE FIRST THREE ROWS OF THIS TABLE ADDITIONALLY GIVE PARAMETERS FOR MASS-RADIUS RELATIONSHIPS COMPUTED FROM THE MODIFIED-POLYTROPIC-EOS; THESE INCLUDE THE  $k_i$  VALUES FOR A FIT TO EQUATION (23) VALID FOR  $M_s > 4$ .

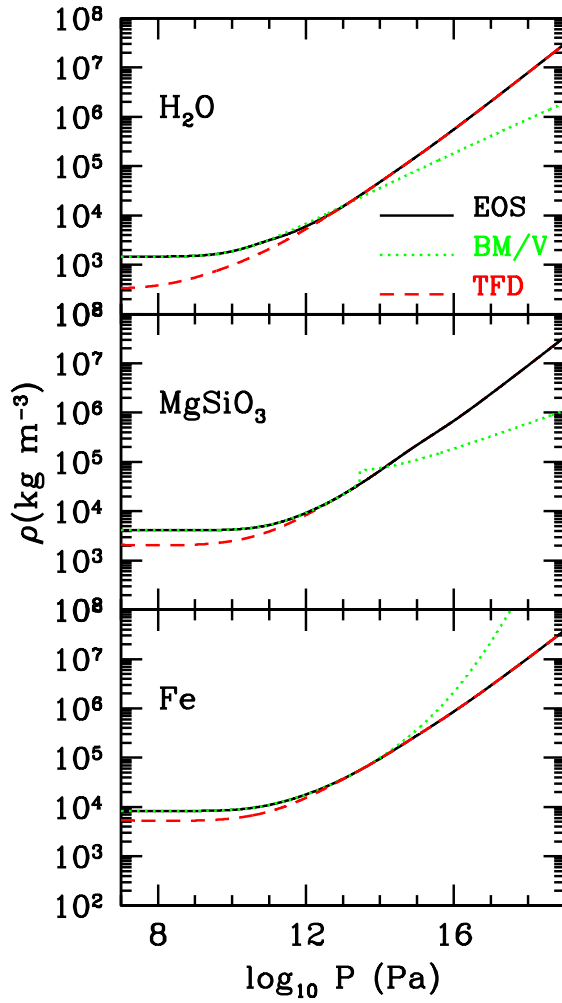


FIG. 1.— Equations of state for different materials at zero or 300 K. The black solid line is the EOS used in this study. The green dotted line is a fit to experimental data (either Vinet (V) or BME (BM)), appropriate for low pressures (typically below 200 GPa). The red dashed line is the TFD EOS, appropriate for high pressures (typically above  $10^4$  GPa). We adopt the Vinet or BME EOS at low pressures and switch to the TFD EOS at high pressures. Note that the abrupt increase in density of the  $\text{MgSiO}_3$  BME curve at  $2.8 \times 10^{13}$  Pa is above the pressure where we switch over to the TFD EOS, and illustrates the invalidity of extrapolating the BME to high pressures.

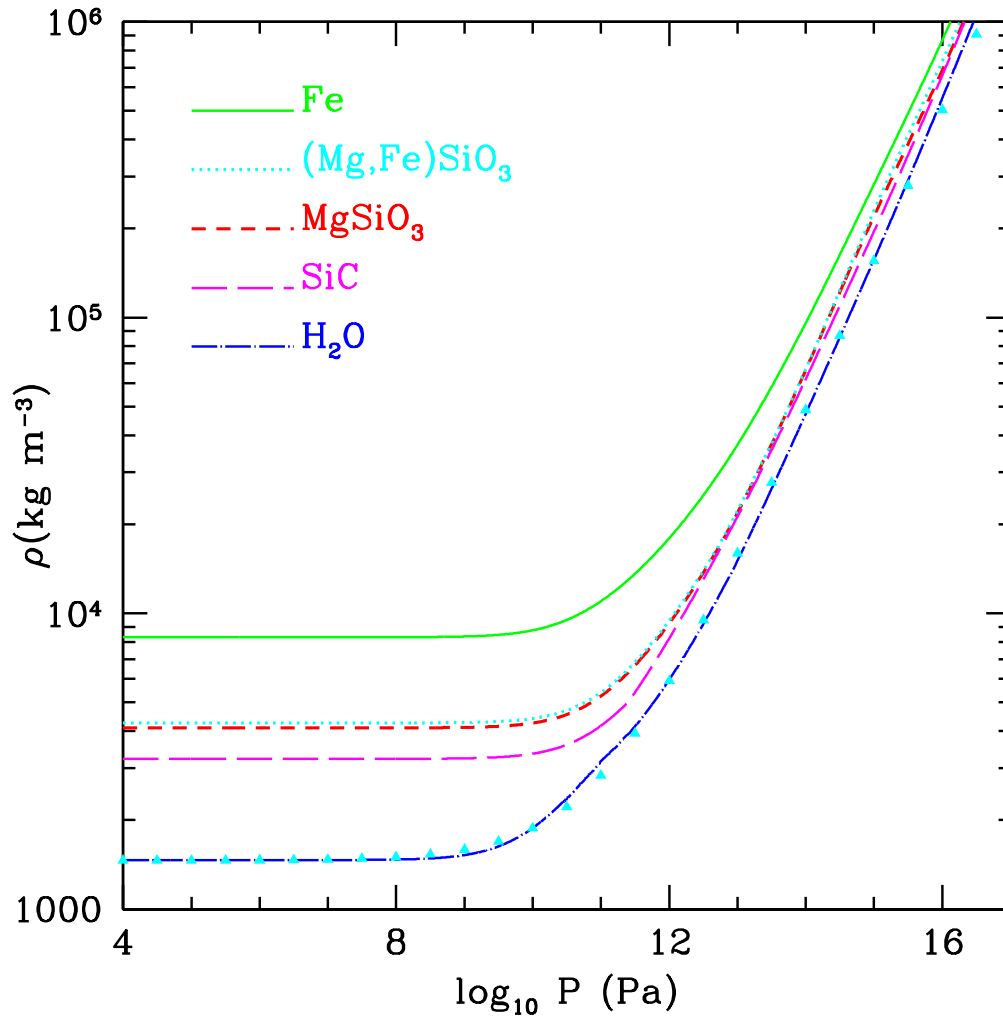


FIG. 2.— Equations of state for five different materials used in this study. Each EOS data set was derived by combining a fit to experimental results and the TFD limit at high pressure. For water ice we used density functional theory as a bridge between experiment and the TFD theory. The EOSs are all reasonably well approximated by a polytropic-like expression  $\rho(P) = \rho_0 + cP^n$ , where  $\rho_0$  is the zero-pressure density and  $c$  and  $n$  are constants. Table 2 lists these constants for some materials. The cyan triangles show one such fit for the  $\text{H}_2\text{O}$  EOS.

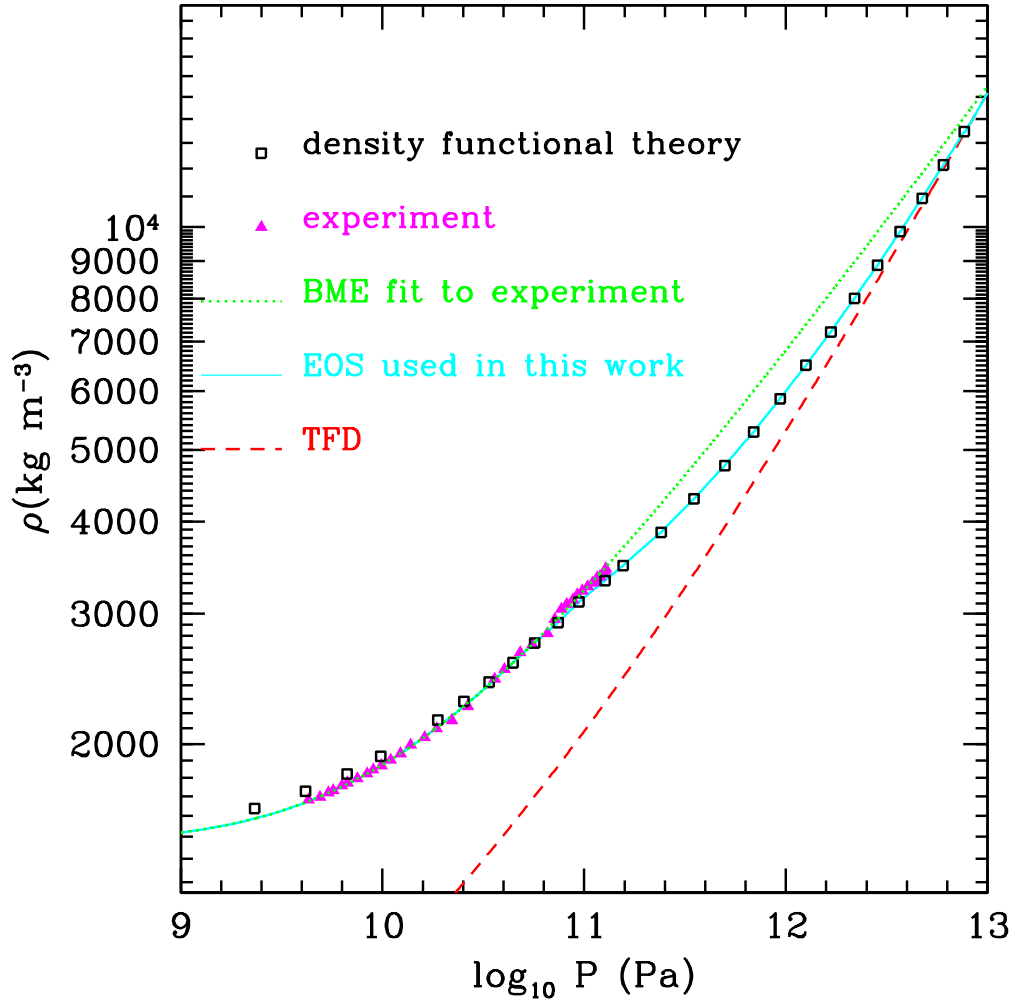


FIG. 3.— The  $\text{H}_2\text{O}$  EOS used in this study (solid cyan curve). We use the BME fit to the experimental data (Hemley et al. 1987, magenta triangles) up to  $P = 44.3$  GPa. At this pressure we switch to the density functional EOS (squares). At  $P = 7686$  GPa we switch to the TFD EOS (red dashed curve).

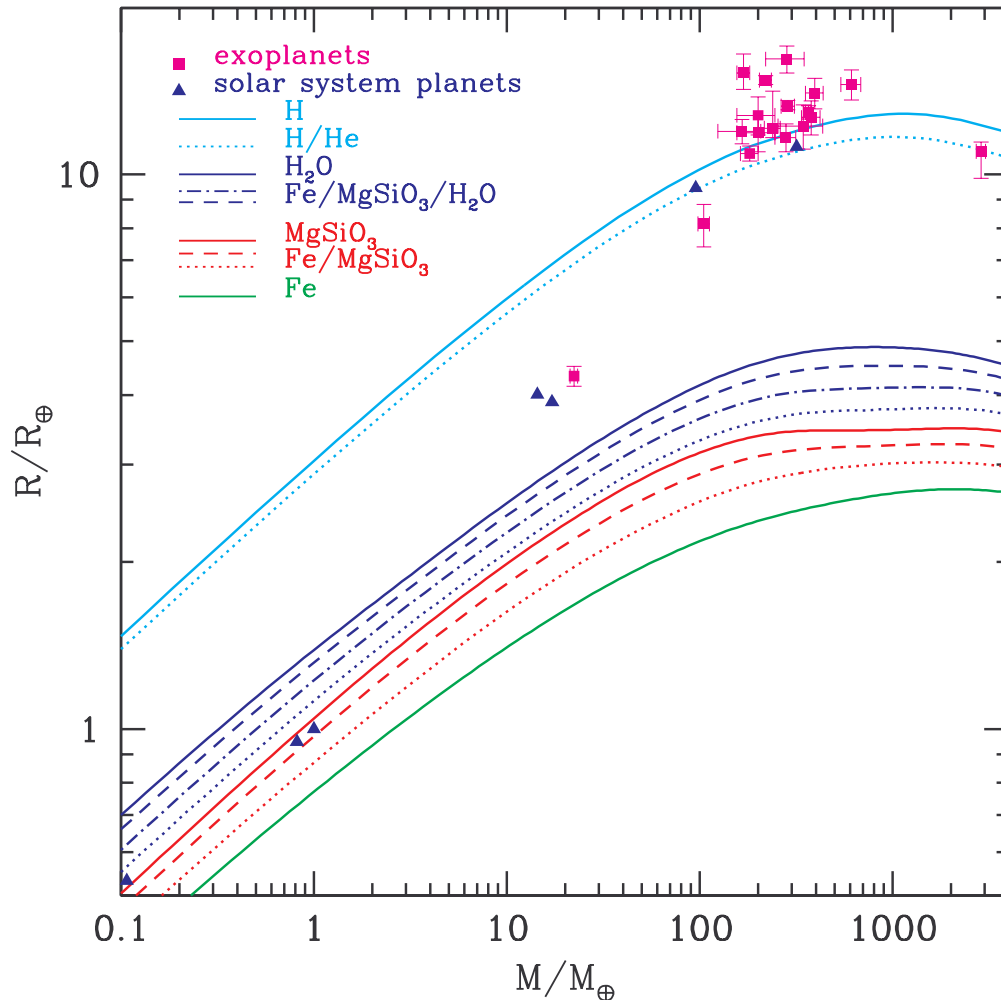


FIG. 4.— Mass-radius relationships for solid planets. The solid lines are homogeneous planets. From top to bottom the homogeneous planets are: hydrogen (cyan solid line); a hydrogen-helium mixture with 25% helium by mass (cyan dotted line); water ice (blue solid line); silicate ( $\text{MgSiO}_3$  perovskite; red solid line); and iron (Fe ( $\epsilon$ ); green solid line). The non-solid lines are differentiated planets. The red dashed line is for silicate planets with 32.5% by mass iron cores and 67.5% silicate mantles (similar to Earth) and the red dotted line is for silicate planets with 70% by mass iron core and 30% silicate mantles (similar to Mercury). The blue dashed line is for water planets with 45% water ice, a 22% silicate shell and a 3% iron core; the blue dot-dashed line is for water planets with 75% water ice, a 22% silicate shell and a 3% iron core; the blue dotted line is for water planets with 25% water ice, a 52.5% silicate shell and a 22.5% iron core. The blue triangles are solar system planets: from left to right Mars, Venus, Earth, Uranus, Neptune, Saturn, and Jupiter. The magenta squares denote the transiting exoplanets, including HD 149026b at  $8.14 R_{\oplus}$  and GJ 436b at  $3.95 R_{\oplus}$ . Note that electron degeneracy pressure becomes important at high mass, causing the planet radius to become constant and even decrease for increasing mass.

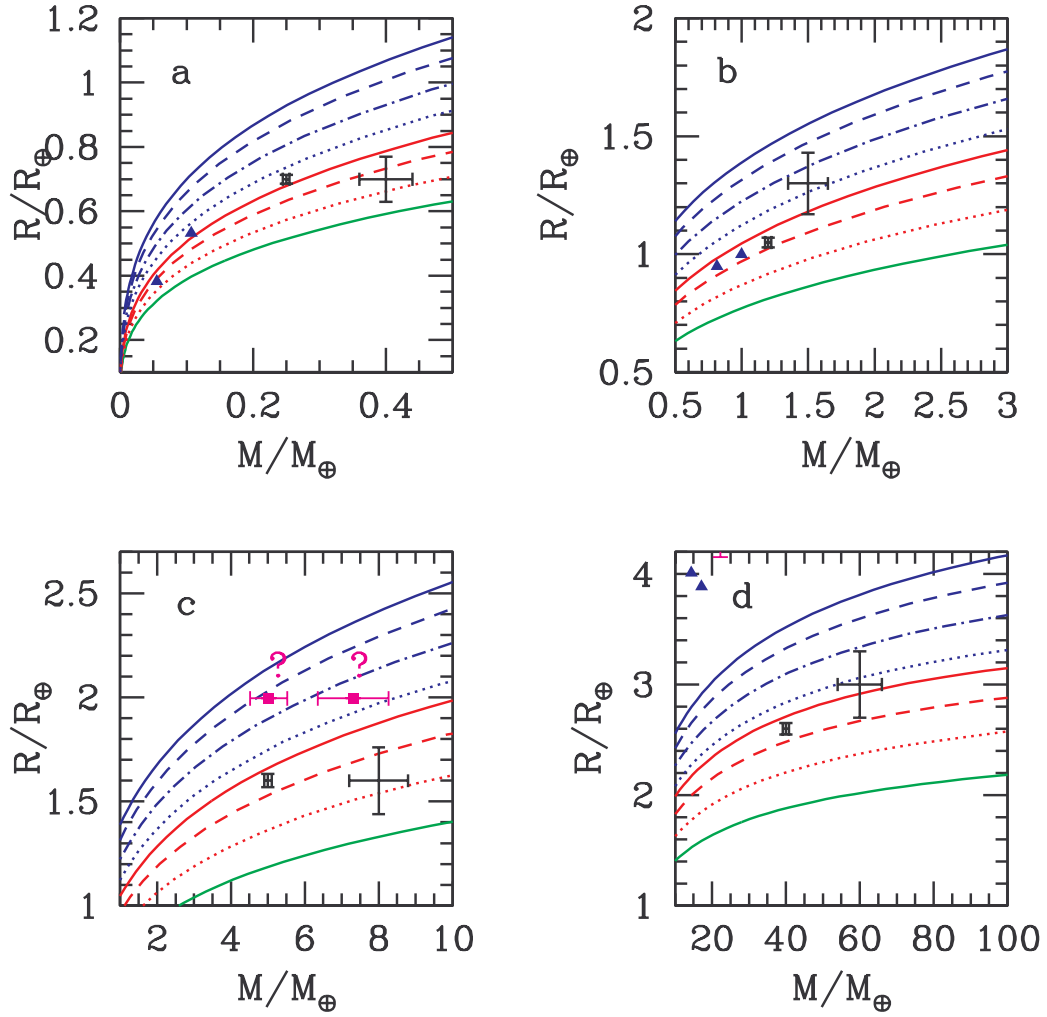


FIG. 5.— Mass-radius relationships for planets with  $R_p < 4R_\oplus$ . The curves are as in Figure 4: blue are for water ice planets, red are for silicate planets, and green is for pure iron planets. Black error bars are shown for 2% and 10% uncertainty in planet mass and radius. Each panel shows a different mass range. The terrestrial-mass solar system planets are shown with blue triangles. The exoplanets Gl 876d and Gl 531c are shown with a magenta square in panel c; although the radii are not known they are shown to represent known low-mass exoplanets. The exoplanet GJ 436b is shown in panel d.

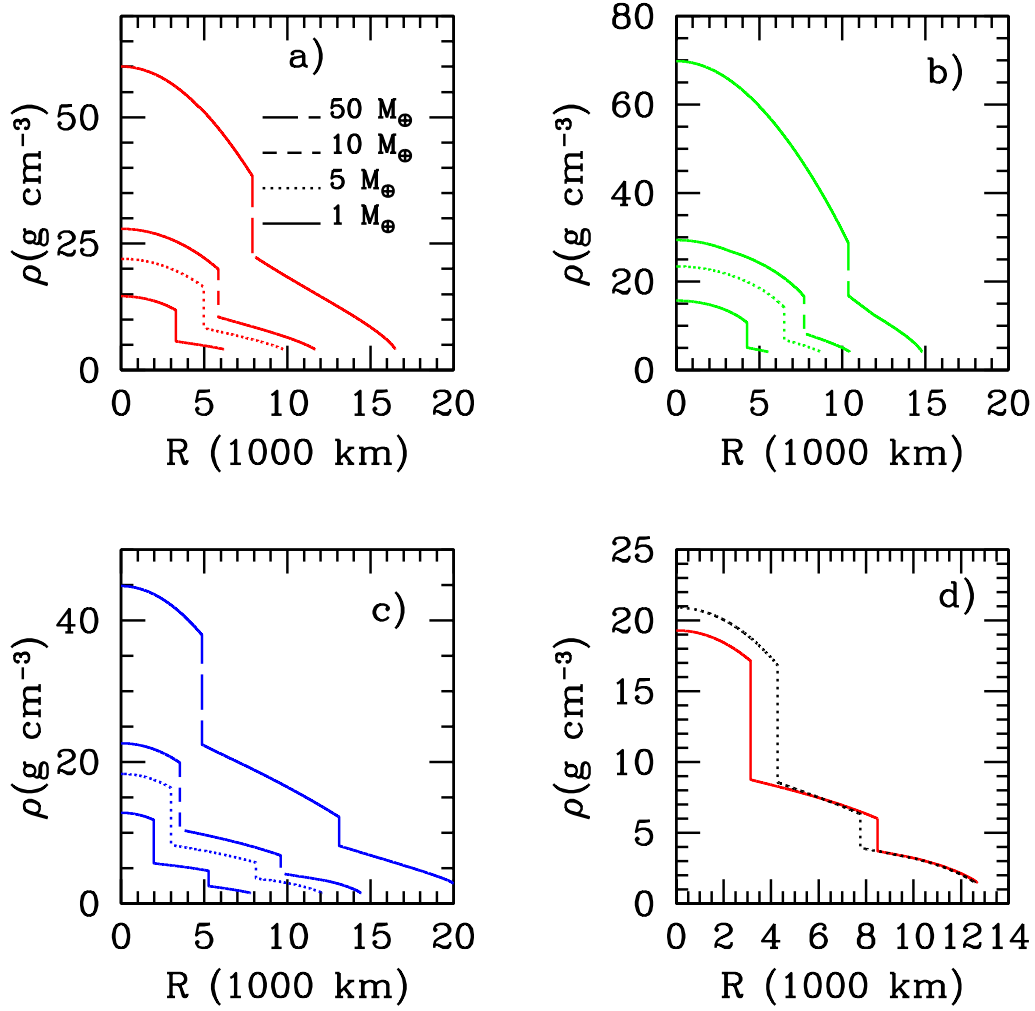


FIG. 6.— Interior structure of solid exoplanets. From top to bottom the curves in panels a, b, and c are for planets with  $M_p = 50, 10, 5,$  and  $1 M_\oplus$  respectively. Panel a: silicate planets with a 32.5% by mass Fe core and a 67.5%  $\text{MgSiO}_3$  mantle. Panel b: as in panel a but for planets with a 70% Fe core and 30% silicate mantle. Panel c: interior structure for water planets with 6.5% Fe core, 48.5%  $\text{MgSiO}_3$  shell, and 45% outer water ice layer. Panel d: interior model for two different water exoplanets with the same planet mass and radius:  $M_p = 6.0 M_\oplus$  and  $R_p = 2.0 M_\oplus$ . The solid curve is for a model with layers in percentages by mass of Fe/ $\text{MgSiO}_3$ / $\text{H}_2\text{O}$  of: 17/33/50 (similar to the composition of the water planet in (Léger et al. 2004)) and the dotted line for 6.5/48.5/45 (similar to the composition of Ganymede).

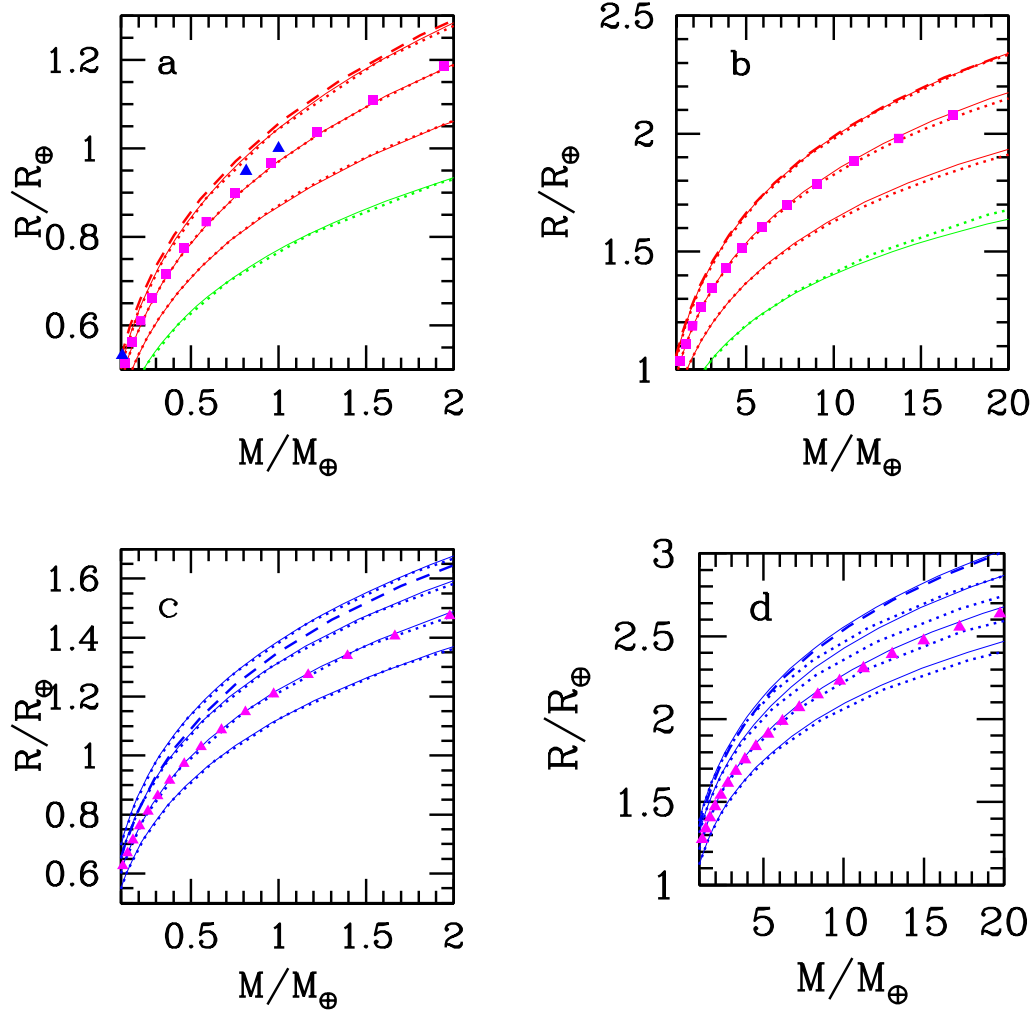


FIG. 7.— Mass-radius relationships of solid planets to illustrate phase effects. Panel a and b: from top to bottom the solid curves are for: pure  $\text{MgSiO}_3$  perovskite planets;  $\text{MgSiO}_3$  planets with a 32.5% by mass  $\text{Fe}(\epsilon)$  core;  $\text{MgSiO}_3$  planets with a 70% Fe core; and pure Fe planets. The dotted lines just above or beneath each of the solid curves is the planet mass-radius relationship for the BME or Vinet EOS alone without the TFD EOS. The top dashed line shows the pure  $\text{MgSiO}_3$  perovskite planet with a phase change to  $\text{MgSiO}_3$  enstatite at pressures less than 10 GPa. The squares show “super Earths” composed of a 32.5 % FeS core by mass and a 67.5% mantle; the mantle itself composed of 90%  $(\text{Mg,Fe})\text{SiO}_3$  by mass mixed with 10% MgO. Panels c and d: from top to bottom the solid lines are water ice planets with layers in percentages by mass of Fe/MgSiO<sub>3</sub>/H<sub>2</sub>O of: 0/0/100; 3/22/75; 6.5/48.5/45, 22.5/52.5/25. The dotted lines beneath each of the solid curves is the planet mass-radius relationship for the BME form of H<sub>2</sub>O ice, without using our adopted H<sub>2</sub>O EOS (but using our adopted EOSs for  $\text{MgSiO}_3$  and Fe). The dashed line shows the pure water ice planet with liquid water below 10 GPa. The magenta triangles show the mass-radius relationship for water planets with 17/33/50, illustrating a degeneracy with the 6.5/48.5/45 water planet (see also Figure 6d).



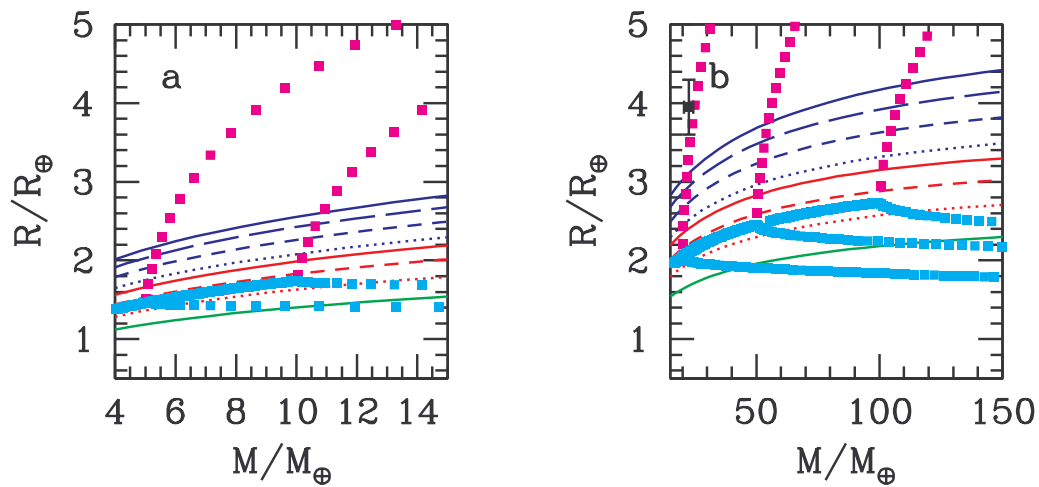


FIG. 8.— The effect of a H/He gas envelope on planet radius, showing that only a small mass of H/He gas contributes a large factor to the planet radius. The lines in this Figure are the same as those in Figure 4. The magenta squares are planets with a fixed core mass composed of a mixture of 30% Fe by mass and 70% MgSiO<sub>3</sub>. The cyan squares show the core mass and radius only. Panel a shows planets with a fixed core mass of 5 $M_{\oplus}$  and 10 $M_{\oplus}$  (from left to right). Panel b shows planets with a fixed core mass of 20 $M_{\oplus}$ , 50 $M_{\oplus}$  and 100 $M_{\oplus}$  (from left to right). These H/He planet radii are underestimates because they are for zero temperature; temperature would make the planets larger for a given mass (i.e. move the squares up and left in this figure).

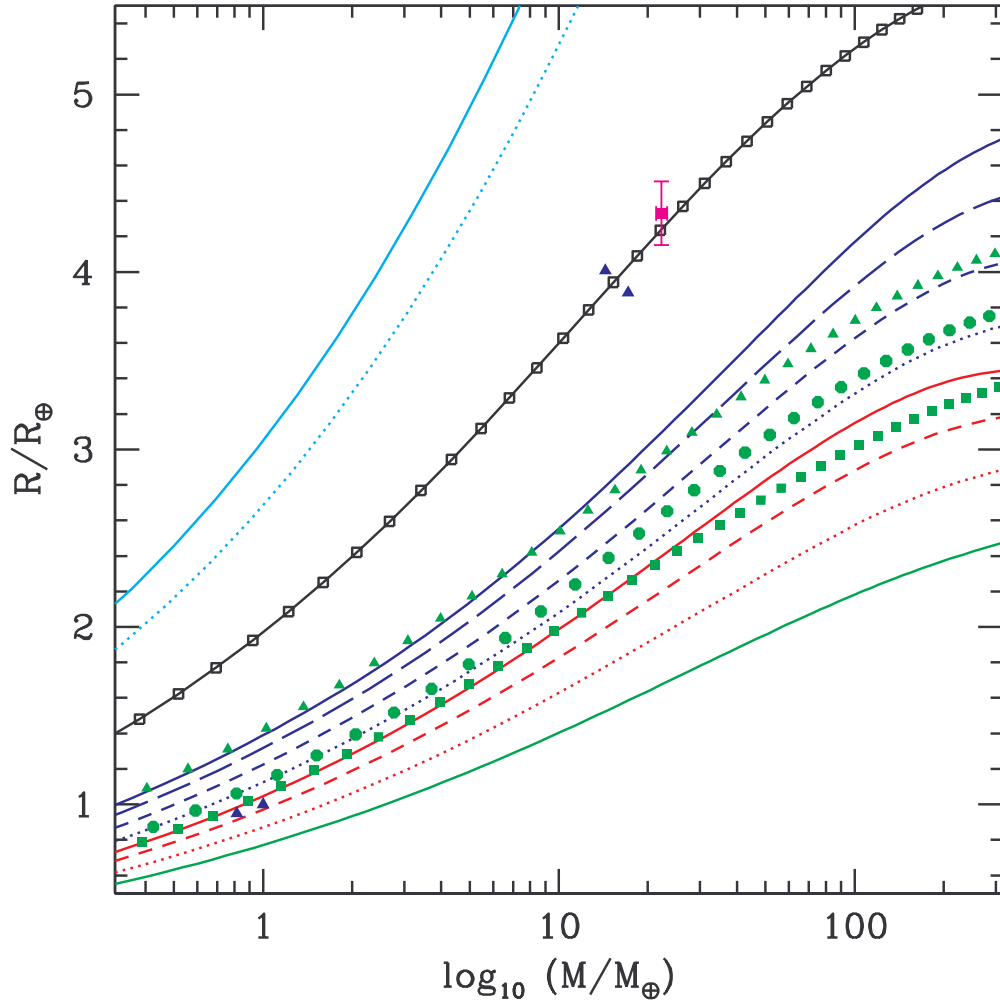


FIG. 9.— Mass-radius relationship for carbon planets and helium planets. The curves are the same as those in Figure 4. The carbon planet mass-radius relationships are shown for: carbon monoxide planets (green triangles); graphite planets with 30% Fe cores by mass and 70% graphite mantles (circles); and SiC planets with 30% Fe cores by mass and 70% SiC mantles (squares). Pure cold He planet mass-radius relationships are shown by open squares connected by a solid line. The solar system planets are shown by the blue triangles.

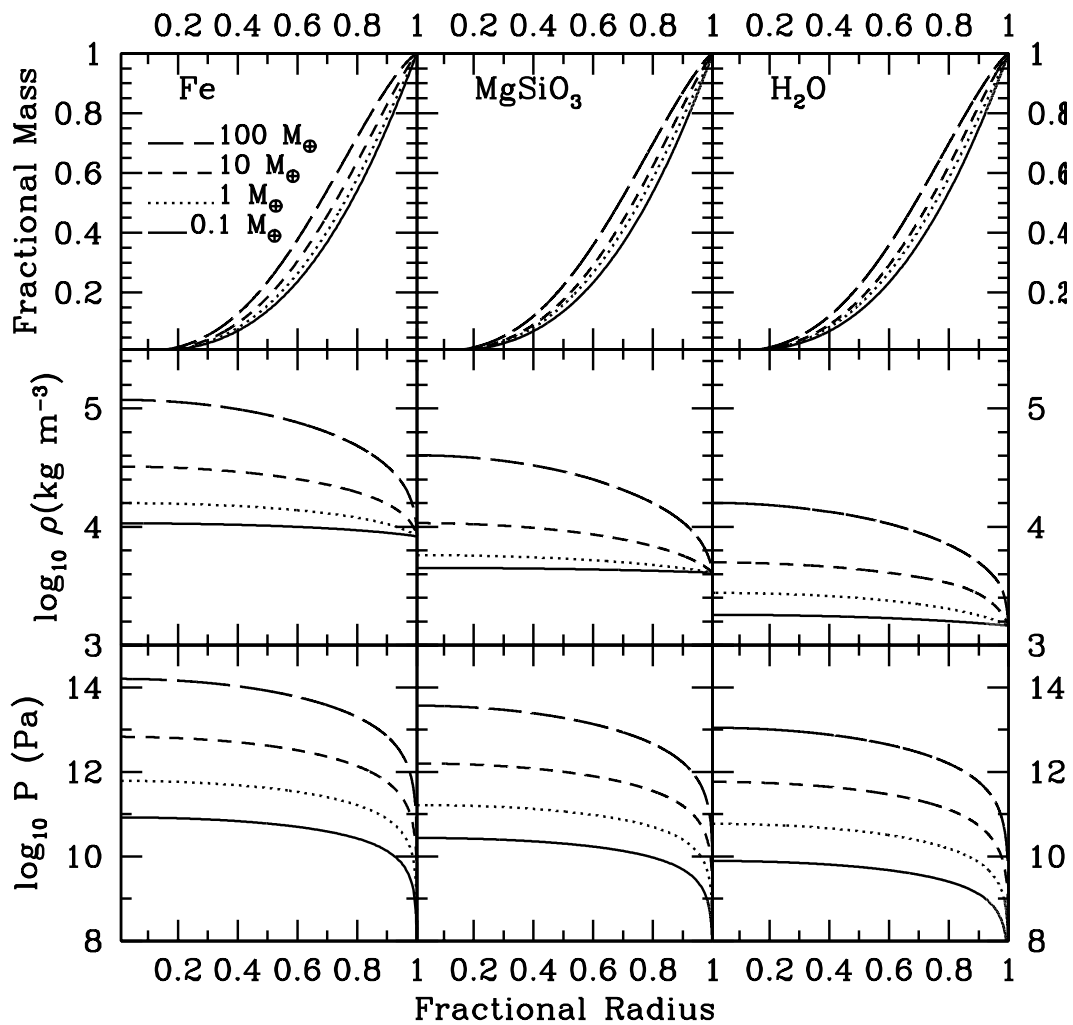


FIG. 10.— Interior structure of homogeneous planets of 0.1, 1, 10, and 100  $M_{\oplus}$ . The top row shows the fractional mass as a function of fractional radius. The middle row shows the density as a function of fractional radius. The bottom row shows the pressure as a function of fractional radius.

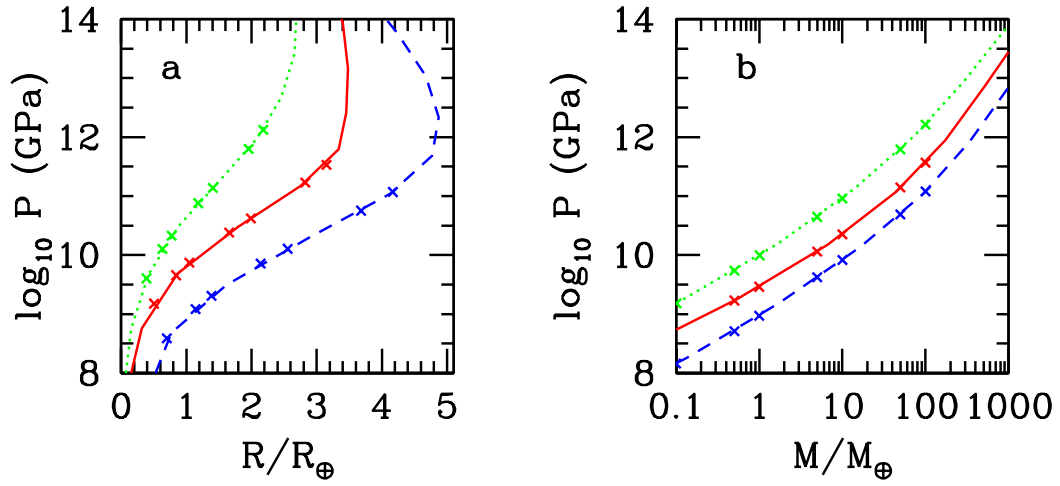


FIG. 11.— The pressure level that contains 97% of the planet radius or mass. Panel a: the pressure at which the planet is 97% of its total size, as a function of total planet radius. Panel b: The pressure at which the planet contains 97% of its total mass, as a function of planet mass. The blue dashed curve is for pure water ice planets, the red solid curve is for pure silicate planet, and the green dotted curve is for pure iron planets, and  $\text{H}_2\text{O}$  ice VII.

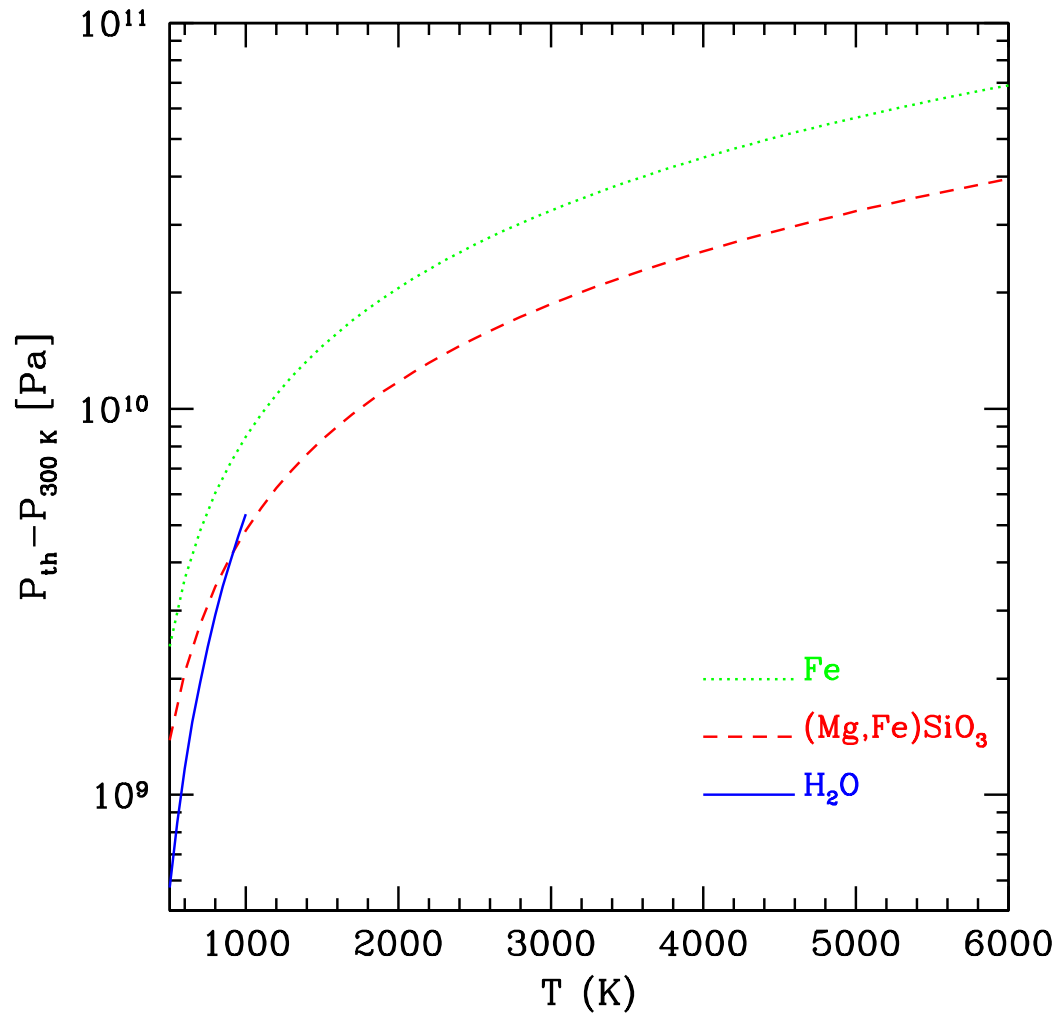


FIG. 12.— Thermal pressure for Fe ( $\epsilon$ ),  $(Mg,Fe)SiO_3$ , and  $H_2O$ . See text for details.

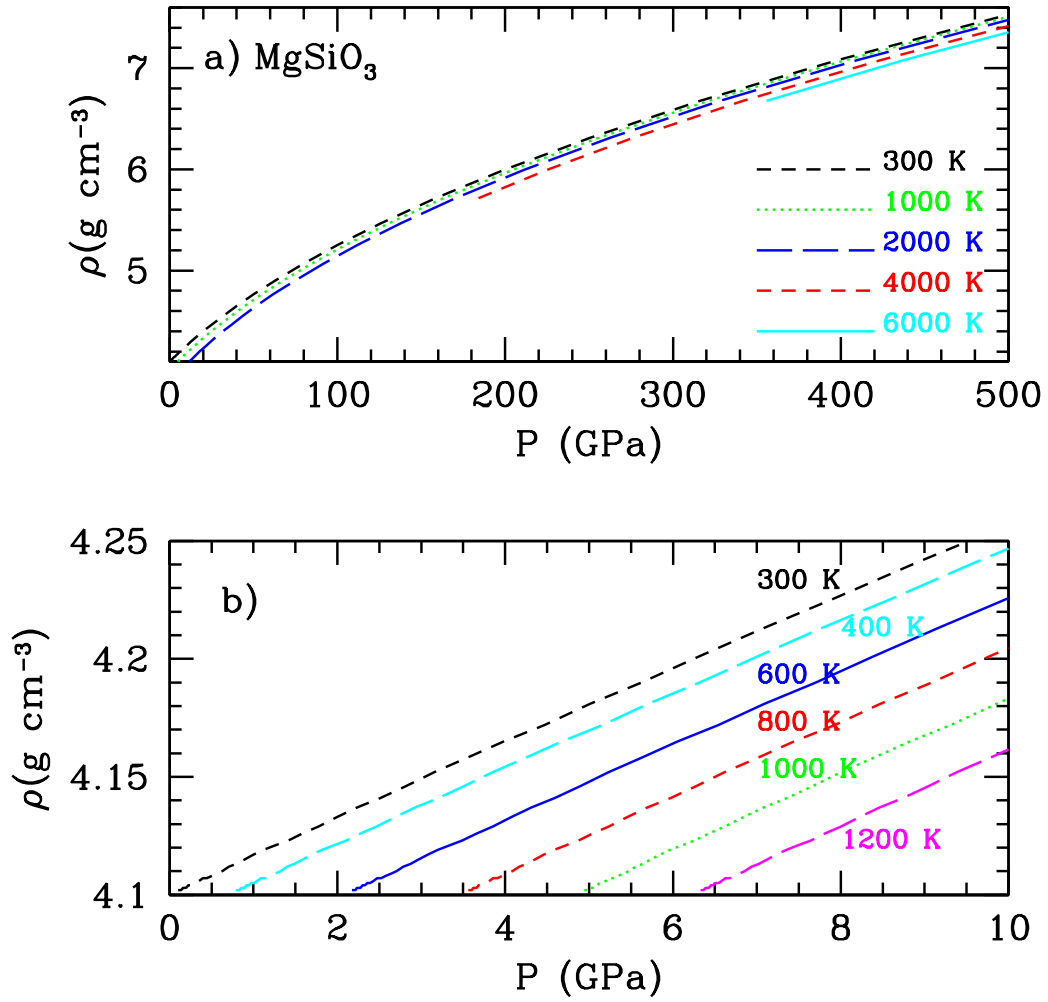


FIG. 13.— Isotherms for MgSiO<sub>3</sub> (perovskite). Note that the perovskite phase of silicate does not exist for the whole region of low pressures shown in panel b, which is therefore shown to illustrate the general properties of silicates.

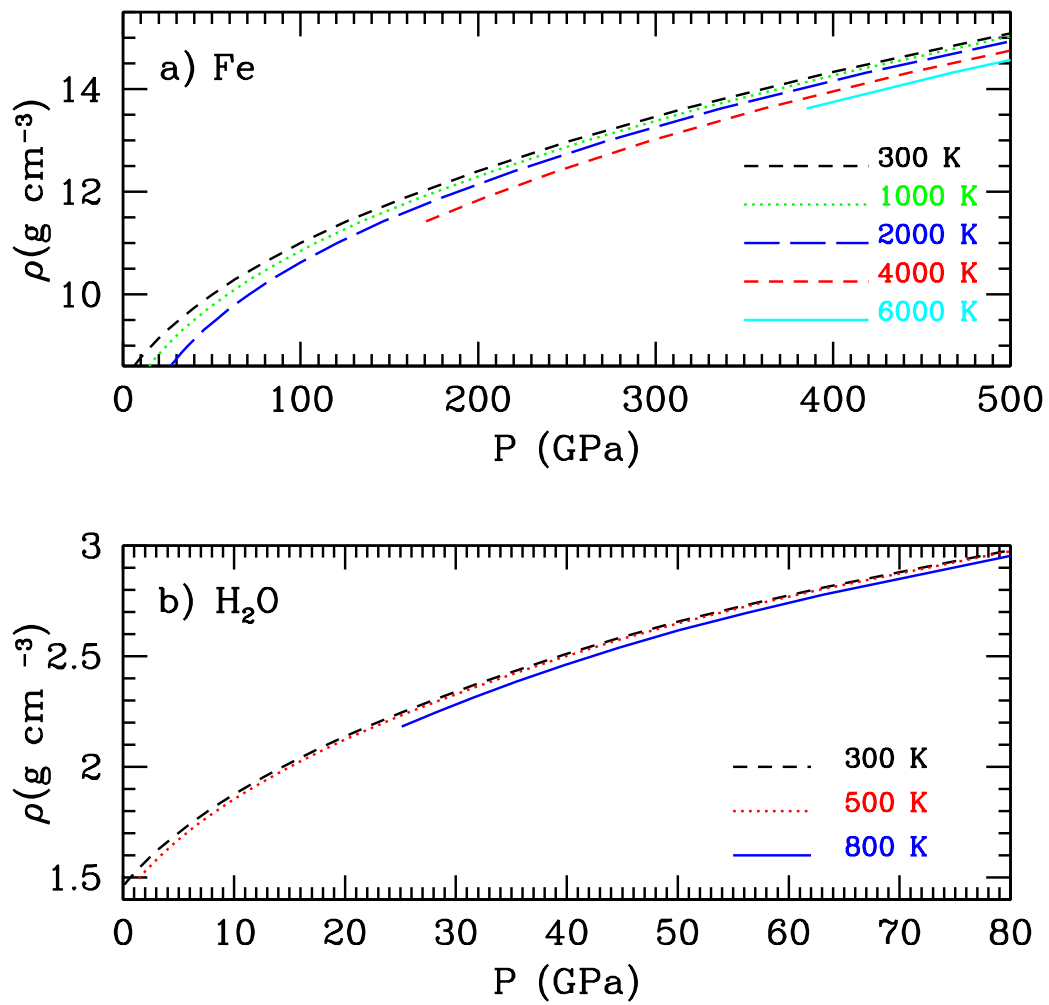


FIG. 14.— Isotherms for Fe( $\epsilon$ ) and H<sub>2</sub>O ice VII. See text for details.

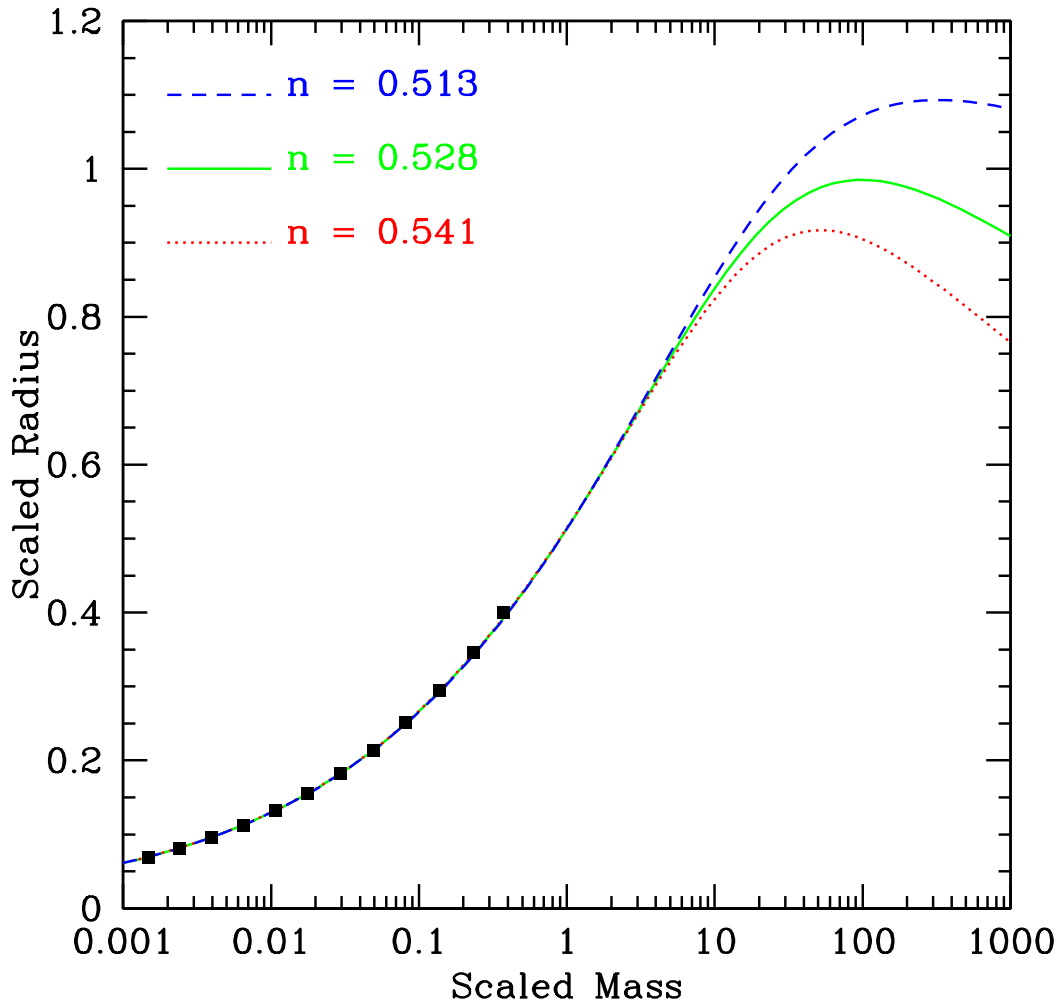


FIG. 15.— Dimensionless mass-radius relationships for different materials. The scaled mass and radius are given in equations (15) and (16). These dimensionless mass-radius relationships depend only on the exponent,  $n$ , in the modified polytrope EOS ( $n = 0.513$  corresponds to the  $\text{H}_2\text{O}$  modified polytrope,  $n = 0.528$  corresponds to Fe, and  $n = 0.541$  corresponds to  $\text{MgSiO}_3$ ). For  $M_s \lesssim 4$ , the mass-radius relationship for all materials takes approximately the same functional form. The squares are the approximate analytical scaled mass-radius relationship given in equation (39), which is valid for  $M_s \ll 1$  and is the same for all  $n$ .



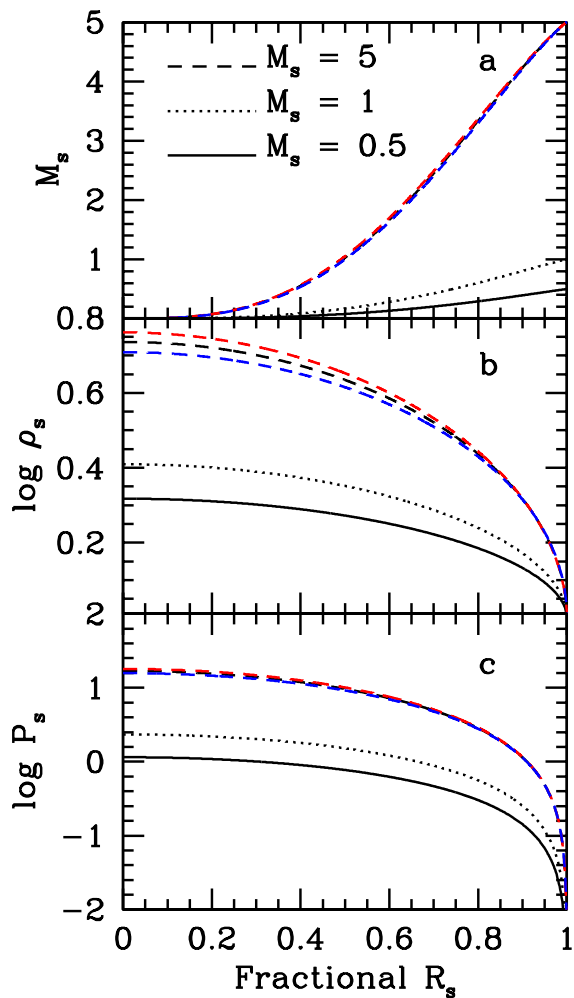


FIG. 16.— Scaled interior structure models for solid exoplanets computed from the polytropic-like EOSs. Panel a: scaled mass vs. fractional scaled radius. Panel b: scaled density vs. fractional scaled radius. Panel c: scaled pressure vs. scaled fractional radius. In all panels the solid, dotted, and dashed curves are for scaled masses of 0.5, 1, and 5, respectively. Three different values of  $n$  are used 0.528 (Fe; black), 0.541 (MgSiO<sub>3</sub>; red), and 0.514 (H<sub>2</sub>O; blue). In all panels the solid and dotted curves are shown for only a single value of  $n$ , because the curves for all  $n$  overlap. The scaled interior structure solutions deviate from each other for the  $M_s = 5$  model.